

Probing semi-macroscopic vacua by high fields of lasers

K. Homma,^{1,2} D. Habs,² and T. Tajima²

¹Graduate School of Science, Hiroshima University, Kagamiyama, Higashi-Hiroshima 739-8526, Japan

²Ludwig-Maximilians-Universität München, Fakultät f. Physik, Am Coulombwall 1, D-85748 Garching, Germany

(Dated: November 11, 2018)

The invention of laser immediately enabled us to detect nonlinearities of photon interaction in matter, as manifested for example by Franken et al.'s detection of second harmonic generation and the excitation of the Brillouin forward scattering process. With the recent advancement in high power high energy laser and the examples of the nonlinearity study of laser-matter interaction by virtue of properly arranging laser and detectors, we envision the possibility of probing nonlinearities of photon interaction in vacuum over substantial spacetime scales compared with the microscopic scale provided by high energy accelerators. The hithertofore never detected Euler-Heisenberg nonlinearities in quantum electrodynamics (QED) in vacuum should come within our reach of detection using intense laser fields. Also our method should put us in a position with a far greater sensitivity of probing possible light-mass fields that have been postulated. With the availability of a large number of coherent photons our suggested measurement methods include the phase sensitive (contrast) imaging that avoids the pedestal noise and the scheme of second harmonic detection of photon nonlinearities in vacuum over a long co-propagating distance incurring resonance excitation. These methods carve out a substantial swath of new experimental parameter regimes of the exploration of photon nonlinearities in vacuum covering the force range from the electron mass scale to below neV.

PACS numbers: 42.50.Pq, 42.65.Ky, 42.65.Es, 14.80.Va, 95.36.+x

I. INTRODUCTION

The invention of laser in 1960 constituted an introduction of the possibility of coherent intense photon fields at the optical wavelengths. In fact immediately following it Franken et al.[1] observed the nonlinearity of the quartz crystal generated second harmonics of the laser at the 'high field' of 10^5 V/cm. Many other nonlinearities of the media due to the high intensity of the laser have been discovered by subsequent years, as compiled in the late 1960's [2]. Above the field of manifestation of the nonlinearity of the second harmonic generation that Franken et al. encountered, neutral atoms may be directly ionized at the field called the Keldysh field [3], which is on the order of 10^8 V/cm (*i.e.* an atomic scale of an eV potential over an Å length), depending on the material. The material's nonlinearities arise from its polarization under a large enough field of laser beyond the linear atomic field strength. See Fig.1(a). Typically the restoring force of the electron to the rest of the atom saturates and can no longer match so much stronger applied field. Relativistically strong lasers (*i.e.* the laser field is so strong to bring electrons to relativistic energies in an optical cycle) can induce the relativistic nonlinearity in electron dynamics of plasma, which is instrumental in producing intense wakefields [4]. This is shown in Fig.1(b). Spurred by the promise and requirement of intense fields that can be sustained in a plasma wakefield excitation, since the invention of the CPA (chirped pulse amplification) [5] the achievable laser intensity has been exponentially multiplying [6]. Along with this advance of most intense laser development comes a technique to further the available laser field such as in [7], which in prin-

ciple sees the possibility of reaching even the Schwinger field characterized by a quantum electrodynamic (QED) scale of an MeV (an electron-positron pair creation energy) over the Compton length, *i.e.* 10^{16} V/cm. Just as the material's ionization happens at the Keldysh field, the vacuum breakdown happens at the Schwinger field [8]. This is depicted in Fig.1(c). Even before reaching this Schwinger field a host of nonlinear behaviors under intense fields are expected [9].

The study of matter and vacuum behaviors under intense fields these days is called high field science and reviews may be found in [6, 9–11]. In the following we suggest a class of possible investigations of vacuum in high field science, where we take advantage of the large amplitude of the (laser) electromagnetic fields and the relatively macroscopic scale of the field spatial scale (typically micron) compared with the microscopic collider experiments (typically fm or less). The most successful tool for exploring the fundamental nature in smallest structures of matter has been that of collider, in which high energy (and thus high momentum) charged particles are produced and collide each other to probe the smallest scale with highest energies ($\delta x \sim \hbar/p$). The present approach we suggest here may be contrasted to this high momentum approach, in that it explores semi-macro spatial scales and relatively lower energy processes with high amplitude (or fields) by '*exciting the constituent matter (or vacuum) and its structure*'.

We may wish to once again borrow the parallelism of the two alternative investigation methods of atomic physics by particle collisions and by laser nonlinear optics. The former explores the atom via Rutherford's method of the high energy beam streaming through and thereby scattered by the constituent matter deep in its

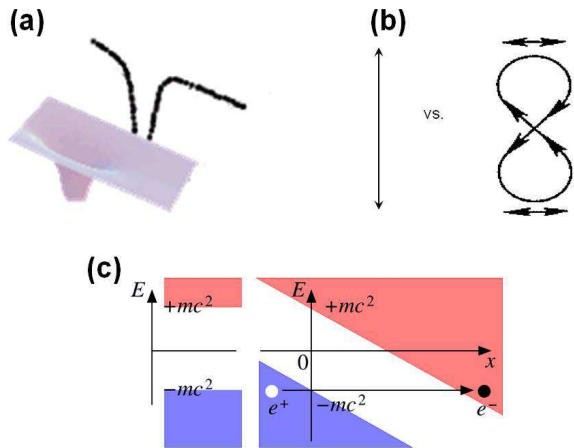


FIG. 1: Photon nonlinearities in media. (a) The nonlinearity arising from atomic anharmonic fields in high intensities; (b) The relativistic nonlinearity of plasma electrons in relativistically intense laser makes the harmonic oscillations of electrons (left) turn into anharmonic motions (right); (c) Even in vacuum photon nonlinearities occur when the field intensity approaches the Schwinger field, at which the intense field can polarize the vacuum anharmonically and eventually help virtual electrons and positrons turn into real particles, a clear manifestation of the breakdown of harmonic photon fields in the low intensity ordinary conditions.

core. By this Rutherford discovered that the ordinary matter is composed of electrons that pervade the unit of the constituent matter, atom, while there exists a tiny core, the nucleus, that sharply scatters the incoming beam. The analysis of the scattering of the injected beam reveals the inner core property. Ever since this epoch making experiment, this approach paved the most successful way of the modern particle physics experimental method, including the collider approach, that can explore ever smaller spatial (and higher energy) structure of the constituent matter. On the other hand, the latter optical approach available only after the invention of laser in 1960 was to excite the atomic electronic structure and carries out spectroscopy of the dynamics. The spectroscopy reveals structure and its dynamical characters by palpating the atom by laser without pinpointed penetration into the core by the beam. This also includes the selective excitation of certain characteristic eigenmodes of the constituent matter structure. A good example may be the method called Laser Induced Breakdown Spectroscopy (LIBS) [12]. When we study the vacuum itself, in stead of neutral atoms, this past experience guides us the distinction of the two approaches the high momentum vs. high field. As the main target of this research, in contrast to the collider's Rutherford approach with high momentum beam scattering, we are now introducing an alternative approach of the method of '*exciting and probing the texture of vacuum*' with high amplitude of photons.

In order to probe such texture or polarization structures of the excited vacuum, we are already treating vacuum as a medium to be studied, rather than a given nothingness. For example, we posit that the phase velocity of light is an experimentally meaningful measurable quantity. Intense photons fields (call it the pump laser or target laser) may provide nonlinearities even in vacuum under a sufficient intensity (whose effects may be probed by another probe laser). Such was predicted by Schwinger [8] in the form of the generation of an electron-positron pair. However, manifestations of nonlinearities and thus the possibility of nonlinear spectroscopy of vacuum should emerge even sufficiently below the Schwinger field threshold. (This may also correspond again to a similar phenomenon of the atomic ionization by intense laser at the Keldysh field and the emergence of atomic nonlinearities far below this Keldysh field.) By this measurement we can investigate the dispersive and birefringence characteristics of photons in the excited vacuum.

Let us consider the constituent's point of view, since the phase velocity shift can also be understood as a result of photon-photon interactions [13–17], as we understood the refractive index in matter through the photon-atom interaction at the level with atoms as the constituent. Photon-photon interactions in vacuum are quantum processes depending on the relevant frequency or mass scales of exchanged fields. Thus, the dispersive nature must be discussed based on the relevant frequency scale we introduce in experiments. As is known from particle physics, in 100 GeV scale we expect that the photon-photon interaction is caused by the heavy neutral boson exchange via higher order fermion loops to couple to photons [22]. As the frequency is lowered, lighter quark and electron loops may cause the photon-photon interaction in the relevant quantum chromodynamics (QCD) and QED mass scales of 100MeV and MeV. Below these scales there is no known mass scale relevant for photon-photon interactions. As long as we use lasers with the eV energy scale with the intensity below the Schwinger limit, therefore, the direct production of real constituent particles is not possible. However, it is possible to discuss virtual vacuum polarizations. This was first introduced by the model through the Euler-Heisenberg effective action [31] on the photon-photon interaction some 70 years ago. Thus far, the real-photon-real-photon interaction has never been experimentally observed. Therefore, when we embark on the study of probing vacuum by optical laser fields, it is one of the first tasks to observe the QED interaction via the measurement of the phase velocity shift under the intense laser field due to this effect.

In addition to exploring the nonlinear QED the current method may introduce a window through which we explore lighter mass scales well below MeV that have been speculated or hinted from particle physics [23, 24] and cosmology [26]. These are related yet unobserved fields of axions and dark energy, for example. We note that the coupling of those light fields to matter must be extremely small. Otherwise, higher energy experi-

ments should have discovered these fields already, since light particles can be copiously produced. Here we recognize an advantage by introducing large amplitude rather than high momentum to search for these light fields that weakly couple to matter. The relevant mass scales of the exchanged fields between photons correspond to the force ranges. Therefore, the study of photon-photon interactions in the low frequency scale below optical frequency may unveil undiscovered semi-macroscopic forces as the basic building block enmeshed in vacuum.

The focus of this paper is to discuss the experimental realization of a new type for the semi-macroscopic scope of vacuum by studying the property of nonlinearities of photons in vacuum. We shall discuss two examples of these. First we suggest an experimental technique of the phase contrast Fourier imaging to measure the phase velocity of photon under strong laser fields in section II and III. This aims at a first verification of the nonlinear QED effect as pronounced by Euler-Heisenberg and beyond. Second we explore a realization of experiments to search for extremely light fields or long ranged force via the resonance interaction, employing quasi-parallel strong laser-laser interaction in section IV, V and VI. In the conclusion section VII, we summarize our approach with high fields of lasers based on a wider perspective by comparing our methods with those in particle collider physics and cosmology.

II. PROBING NONLINEAR QED AND BEYOND

Maxwell's equations suggest linear superposition of photons. On the other hand, the quantum electrodynamics (QED) indicates a weak interaction of photon-photon through the Feynmann's diagram of the box type, where a virtual electron-positron pair loops and four real photons couple to the loop at the four vertexes as external lines (see Fig.7(b)). The photon-photon scattering cross section based on the box diagram is calculated by [28, 29]. The total elastic cross section in the center of mass system with the photon energy of ω is expressed as

$$\sigma_{\text{qed}} = \frac{973}{10125\pi} \alpha^2 r_e^2 \left(\frac{\hbar\omega}{m_e c^2} \right)^6, \quad (1)$$

where $\alpha = \frac{e^2}{\hbar c}$ is the fine structure constant, m_e is electron mass and $r_e = \alpha \frac{\hbar c}{m_e c^2} \sim 2.8 \times 10^{-13}$ cm is the classical electron radius. For photons of $\hbar\omega \sim 1$ eV, the cross section is 10^{-42} b. This is extremely small. The smallness of this cross section arises from the electron-positron mass scale of the four propagators in the loop of the box diagram or from the short distance nature due to the corresponding Compton wavelength of electron-positron pair. We note that because of this smallness we have little 'noise', providing a pristine experimental environment to search for something beyond QED. In reverse if we do detect any signals in photon-photon interactions,

we are assured of something significant. When one is interested in observing the events of QED real-photon-real-photon scattering itself, the introduction of higher frequency photons as a probe beam onto a high intense optical laser target would have a greater probability due to the $(\hbar\omega)^6$ behavior than the optical-optical photon interaction. In such an asymmetric colliding system, even elastic collisions in the corresponding center-of-mass system (CMS) can be detected as frequency shifted scattered photons in the laboratory frame, depending on the collision geometry with reasonably high statistics. Furthermore, in such a setup, the non-perturbative nature of the intense field is expected to be important. For example, the catalysis of electron-positron pair production [30] due to a higher tunneling probability from the Dirac sea may be tested, even below the Schwinger field [8].

In what follows we discuss on the measurement of the phase velocity shift, where we focus on the optical-optical beam interaction. The strong electromagnetic field may modify the dispersion relation for photons. This effect is first discussed by Toll [13]. If we detect the predicted velocity shift explained below, it amounts to the verification of the nonlinear QED effects in the perturbative regime. In the low frequency collision it is sufficient to describe the photon-photon interaction by the effective one-loop Lagrangian [8, 31, 32]

$$L_{1-loop} = \frac{1}{360} \frac{\alpha^2}{m_e^4} [4(F_{\mu\nu}F^{\mu\nu})^2 + 7(F_{\mu\nu}\tilde{F}^{\mu\nu})^2], \quad (2)$$

where $F_{\mu\nu} = \partial A_\mu / \partial x^\nu - \partial A_\nu / \partial x^\mu$ is the antisymmetric field strength tensor and its dual tensor $\tilde{F}^{\mu\nu} = 1/2 \epsilon^{\mu\nu\lambda\sigma} F_{\lambda\sigma}$ with Levi-Civita symbol $\epsilon^{\mu\nu\lambda\sigma}$. It is well known that the forward scattering amplitude f with the dimension of length is related to the refractive index n via the Lorentz relation [33]

$$n(\omega) = 1 + \frac{2\pi}{(\omega/c)^2} N f(\omega), \quad (3)$$

where N is the number density of scattering centers and $f(\omega)$ is the forward scattering amplitude for light of energy $\hbar\omega$. The total cross section σ is related to the absorptive part of the forward scattering amplitude via the Optical Theorem, as follows

$$\sigma = \frac{4\pi}{\omega/c} \text{Im} f(\omega). \quad (4)$$

If we use a strong coherent electromagnetic field with large N , the real part of the forward scattering amplitude is expected to become large. This is because the coherent addition of the scattering amplitudes over large N is expected. Therefore, we are interested in the measurement of the refractive index shift under the high electromagnetic field. It is not as effective to focus laser to cause non-forward scattering processes. The refractive index corresponds to the inverse of phase velocity. The derivation of these quantities in the linearly polarized

electromagnetic field target (so called crossed-field configuration where electric field \hat{E} and magnetic field \hat{B} are perpendicular with the same strength) is originally studied in [14, 15] and further derived from the generalized prescription based on the polarization tensor applicable to arbitrary external fields in [16]. This shows us

$$\begin{aligned} v_{\parallel}/c &= 1 - \frac{8}{45} \frac{\alpha^2}{m_e^4} \frac{\hbar^3}{c^5} \frac{z_k}{k^2}, \\ v_{\perp}/c &= 1 - \frac{14}{45} \frac{\alpha^2}{m_e^4} \frac{\hbar^3}{c^5} \frac{z_k}{k^2}, \end{aligned} \quad (5)$$

where v_{\parallel}/c and v_{\perp}/c are the phase velocities when the combination of linear polarizations of the probe and target lasers is either parallel and perpendicular, respectively. The quantity $m_e^4 c^5 / \hbar^3 \sim 1.42 \times 10^{24} \text{J/m}^3$ is the Compton energy density of an electron, k is the wave number of the probe electromagnetic field with the unit vector of \hat{k} . The Lorentz invariant quantity z_k is defined as

$$z_k = (k_{\alpha} F^{\alpha\kappa})(k_{\beta} F_{\kappa}^{\beta}), \quad (6)$$

and the relation to the energy density ϵ^2 in the crossed field condition is

$$\frac{z_k}{k^2} = \epsilon^2 (1 + (\hat{k} \cdot \hat{n})^2), \quad (7)$$

with $\epsilon = E = cB$ and $\hat{n} = \hat{B} \times \hat{E}$. Thus the second terms in (5) show the deviation of the phase velocities of light v_{\parallel} and v_{\perp} are proportional to the field energy density normalized to the Compton energy density of an electron.

The shift of the refractive index from that of the normal vacuum is on the order of 10^{-11} for the energy density ϵ^2 of $1 \text{J}/\mu\text{m}^3$. The refractive medium has the polarization dependence, *i.e.* the birefringence nature. The difference in v_{\parallel} and v_{\perp} in (5) results from the first and second terms in the bracket of the effective one loop Lagrangian in (2). The UV limit ($\omega \rightarrow \infty$) of the dispersion and birefringence under a constant electromagnetic field may be evaluated via the Kramers-Kronig dispersion relation, as discussed in [17]. The phase velocity in both UV and IR limits is expected to be subluminal ($v_{\text{phase}} < c$) under the QED field [16, 17]. The UV limit of the phase velocity is supposed to govern causality. Therefore, it can be a fundamental test of a variety of effective field theories in the IR limit whether the phase velocity in the UV limit extrapolated from that of IR is superluminal ($v_{\text{phase}}(\infty) > c$) or not. Thus far the dispersion relation from IR to UV is theoretically known only in the QED field [17]. However, there has never been data even in IR frequencies to date. It is important, therefore, for experiments to quantitatively verify or disprove the QED prediction. We note that the measurement of the refractive index in higher frequency may be sensitive to the part of the anomalous dispersion as discussed in [18] and also the measurement of the electron-positron pair creation [19–21, 30] in

strong electromagnetic field may be directly sensitive to the absorption or imaginary part. The Kramers-Kronig relation connects between the real and imaginary parts of the forward scattering amplitude or the refractive index. Therefore, the systematic measurements of real and imaginary parts over wide frequency range may provide a test ground of QED and the Kramers-Kronig relation itself when it is applied to vacuum.

Suppose then the detected dispersion and birefringence quantitatively deviate from the expectation of QED. This should indicate that undiscovered fields may be mediating photons beyond QED. Scalar and pseudoscalar types of fields may appear via the first and second products in brackets of (2), respectively as we discuss section IV in detail. In addition if masses of scalar and/or pseudoscalar fields are light, this long distance nature may enhance the coherence nature and thereby the amplitude of the forward scattering compared to the lowest order QED diagram. Therefore, the measurement of the birefringence and the comparison to the expectation from the nonlinear QED effects may be a general probe to investigate the fundamental nature of vacuum.

III. PHASE CONTRAST FOURIER IMAGING ON THE FOCAL PLANE

We now consider an experiment where we create a high intensity spot by focusing a laser in vacuum and we probe its refractive index shift by a second laser. We call the first laser as the target laser, while the second as the probe laser hereon. The key issue is to detect an extremely small refractive index change resulting from the photon-photon interaction between the target and probe lasers. The conventional way that was already performed [34] and proposed [35, 36] is based on the measurement of the ellipsoid caused by birefringence and that of the rotation angle of a linearly polarized probe laser by making it propagate for a long distance under a weak magnetic field[34] or electromagnetic field [35, 36]. This method has an advantage to enhance the phase shift by a long optical path without introducing costly strong target electromagnetic fields. In the case of the constant magnetic field on the order of 1T, one encounters the limit of physical detectability sensitive to the QED nonlinear effect. In the case of strong electromagnetic field, one runs into the damage limit to store the strong target field within a cavity over a long time. On the other hand, if we can directly utilize the local nature of vacuum by tightly focusing an intense laser pulse and measuring the lensing effect of vacuum on the pulse-by-pulse basis, there is no physical limit in increasing the intensity of the laser pulse until vacuum itself breaks down. In order to increase the shift in the refractive index corresponding to the inverse of phase velocities in (5), *i.e.* the intensity of the target laser field as expected through (6) and (7), it is necessary to use a focused laser pulse by confining a large laser energy into a small spacetime volume. This

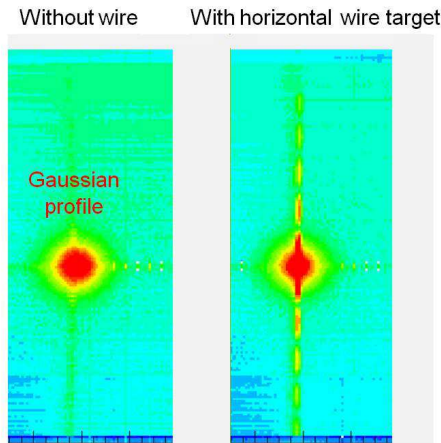


FIG. 2: Diffraction images at the far distance from the thin wire target when the Gaussian laser is shot on the wire. The left figure is the case there is no wire. The right figure is the case when the thin wire target is horizontally arranged.

causes a locally different refractive index along the trajectory of the target laser pulse in vacuum. A variation of the refractive index arises over the high intense part and the rest of vacuum. If the probe laser penetrates into both parts simultaneously, the corresponding phase contrast should be embedded in the transverse profile of the same probe laser. Our proposal is to directly measure the phase contrast and to determine the absolute value of the refractive index change by controlling the combination of polarizations of the probe and target laser pulses. This should result in the birefringence as expected in (5).

We need to detect the extremely small shift of phase velocity by the target-probe interaction. For this we also need an intense probe laser in order to enhance visibility. However, if we utilize the conventional interferometer techniques providing a homogeneous phase contrast over the probe laser profile, such small refractive index changes are hard to detect. This is because the resulting intensity modulation is always on top of the huge pedestal intensity and the contrast of the modulation to the pedestal is extremely small. Any photo device cannot be sensitive to a small number of photons spatially modulating under the pedestal intensity beyond 1J ($\sim 10^{19}$ visible photons) due to the limit of the dynamic range on the photon intensity measurable by a camera pixel without causing saturation on the intensity measurement. On the other hand, broadening the dynamic range by lowering the gain of the electric amplification of photo-electron degrades the sensitivity to the small number of the spatially modulating photons or the sensitivity to the small phase shift. Therefore, we need to invent a method that can spatially separate the weakly modulating characteristic intensity pattern from the strong pedestal.

In order to overcome this difficulty, we suggest utilizing the inhomogeneous phase contrast Fourier imag-

ing on the focal plane by focusing the probe laser via a conceptual lens. In this the physically embedded phase contrast on the transverse profile of the probe laser amplitude is Fourier transformed on the focal plane. The intensity pattern on the focal plane has a preferable feature that the characteristic phase boundary makes the intensity profile expand outer regions far from the focal point, whereas a Gaussian laser with a homogeneous phase converges into a small focal point with the smallest beam waist. It is instructive to illustrate the characteristic nature of the diffraction pattern from a wire-like target shape as shown in Fig.2. Here the intensity pattern at a far distance known as the Fraunhofer diffraction limit is shown in the case when a Gaussian laser beam is shot on the thin wire target. The intensity pattern at a far distance can be understood as the Fourier transform of the wire shape approximated as a rectangular of $2\mu \times 2\nu$. It is well known that a lens component by itself also has the equivalent effect to produce a diffraction pattern corresponding to the exact Fourier transformed image of the original shape of the refractive medium on the focal plane at a finite distance (see [38] for instance). In order to understand the diffraction image, we may refer to Babinet's principle which states that the diffraction pattern from an opaque wire is identical to that from a slit of the same size and shape. The Fourier transform of such a rectangular slit is expressed as

$$\left(\frac{\sin(\mu\omega_x)}{\mu\omega_x} \right)^2 \left(\frac{\sin(\nu\omega_y)}{\nu\omega_y} \right)^2, \quad (8)$$

where $\omega_x = \frac{2\pi}{\lambda f}x$ and $\omega_y = \frac{2\pi}{\lambda f}y$ are the spatial frequencies for the given position (x, y) on the focal plane with the focal length f and the wavelength λ . In the case of the slit with $\mu \gg \nu$, the rectangular profile on the focal plane becomes orthogonally rotated thinner line shape with oscillations included in the line (see Fig.2 (right)). This is because the narrower the slit size is, the smaller the spatial frequency in that direction becomes. On the other hand, the shape of Gaussian distribution without the wire or slit is unchanged, because the Fourier transform of the Gaussian distribution corresponds to the Gaussian distribution (see Fig.2 (left)). This is the key feature that drastically improves the detectability to the small phase shift by sampling only outer parts far from the Gaussian part. This may also be interpreted as the counter-concept to the conventional spatial filter, where outer parts are eliminated to maintain a smooth phase on the transverse profile of the Gaussian distribution.

Given the intuitive picture above, a quantitative formulation of our proposed method is presented as follows. First, let us define the geometry of the laser intersection, as shown in Fig.3 (left), where the tightly focused target pulse with time duration τ_t propagates along the Z -axis and the probe pulse with the larger profile and longer time duration τ_p propagates along the z -axis tilted by θ from the Z -axis. In this figure the wavefronts of the probe pulse are drawn successively with time step τ_t under the condition $\tau_p > \tau_t$. Since the constant phase shift

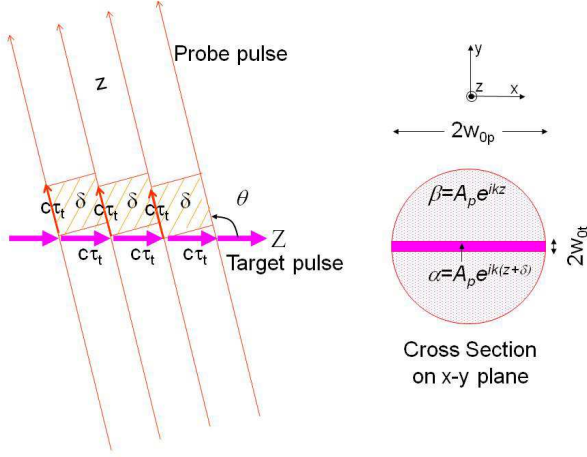


FIG. 3: Geometry of the embedded phase contrast in the probe pulse.

is embedded only during τ_t , the optical length with the constant refractive index shift along the z -axis perpendicular to the wavefront is limited to $c\tau_t$. This is independent of θ . In this geometry after the penetration of the probe laser pulse, the profile of the probe laser on the $x-y$ plane contains a trajectory with the constant phase shift δ along the projection of the path of the target laser on the probe wavefront, as shown in Fig.3 (right).

In order to discuss the amount of the phase shift, we need a concrete geometry at the diffraction limit of both target and probe lasers. Let us briefly review the laser profile at the diffraction limit. The Gaussian profile is a basic constraint in typical laser fields, where the aperture of a lasing material has a finite size in the transverse area. The solution of the electromagnetic field propagation in vacuum with the Gaussian profile on the transverse plane with respect to the propagation direction z is well-known[40]. The electric field component in spatial coordinates (x, y, z) is expressed as

$$E(x, y, z) \propto \frac{w_0}{w(z)} \exp \left\{ -i[kz - \eta(z)] - r^2 \left(\frac{1}{w(z)^2} + \frac{ik}{2R(z)} \right) \right\}, \quad (9)$$

where $k = 2\pi/\lambda$, $r = \sqrt{x^2 + y^2}$, w_0 is the minimum waist which cannot be smaller than λ due to the diffraction limit, and other definitions are as follows:

$$w(z)^2 = w_0^2 \left(1 + \frac{z^2}{z_R^2} \right), \quad (10)$$

$$R = z \left(1 + \frac{z_R^2}{z^2} \right), \quad (11)$$

$$\eta(z) = \tan^{-1} \left(1 + \frac{z}{z_R} \right), \quad (12)$$

$$z_R \equiv \frac{\pi w_0^2}{\lambda}. \quad (13)$$

Let us express the phase shift δ in the limit $z = c\tau_t < z_R$, where we assume an almost flat wavefront as indicated by (10) and (11) in the vicinity of the diffraction limit

$$\delta = \frac{2\pi}{\lambda_p} \delta n_{qed} c\tau_t \varphi_t(x_p, y_p), \quad (14)$$

where the subscripts p and t denote the *probe* and *target* quantities, respectively, δn is the refractive index shift, $c\tau_t$ is the path length with effectively constant phase shift δ over the crossing time τ_t and $\varphi_t(x_p, y_p)$ is a weight function to reflect the path length difference depending on the incident position with respect to the target profile expressed as a function of position (x_p, y_p) on the transverse plane of the probe laser. Based on (5), (6) and (7) we parametrize the refractive index shift as

$$\delta n_{qed} = \zeta N_0 (1 - \cos \theta) \frac{E_t}{\pi w_{0t}^2 c\tau_t}, \quad (15)$$

where ζ is 4 and 7 for the polarization combinations \parallel and \perp , respectively, N_0 is the coefficient to convert from energy density to refractive index shift defined as $N_0 \equiv \frac{2}{45} \frac{\alpha^2 \hbar^3}{m^4 c^5} = 1.67 \times 10^{-12} [\mu\text{m}^3/\text{J}]$, θ is the incident angle of the probe pulse with respect to the propagation direction of the target pulse as depicted in Fig.3, E_t is the energy of the target pulse in [J], and $\pi w_{0t}^2 c\tau_t$ is the volume in $[\mu\text{m}^3]$ for the given target profile with the minimum waist w_{0t}^2 from (10). By substituting (15) into (14) we obtain the experimentally convenient expression for δ

$$\delta \sim \frac{2\pi}{\lambda_p} \zeta N_0 (1 - \cos \theta) \frac{E_t}{\pi w_{0t}^2} \varphi_t(x_p, y_p). \quad (16)$$

We are interested in an application in the limit $w_{0t} < w_{0p}$ for the width and $c\tau_t < w_{0p}$ for the depth of the embedded phase shape. We then take the approximation $\varphi_t(x_p, y_p) \sim 1$ to simplify the following argument (if necessary, we may restore the target profile $\varphi_t(x_p, y_p)$ based on the precise profile of the target laser reflecting actual experimental setups). In this limit we approximate that the target profile has a rectangular shape with the size of $2\mu \times 2\nu$ inside which a constant phase shift is assigned, where the effective slit sizes are defined by the transverse sizes of focused laser beams through the relation $\mu \sim w_{0p}$ and $\nu \sim w_{0t}$. We note that the optical length $c\tau_t$ with phase shift δ of the probe laser is eventually canceled out based on (16). This indicates that we have many choices on τ_t as long as the conditions $c\tau_t < z_{Rt}$ and $\tau_t < \tau_p \sim z_{Rt}/c$ are satisfied.

We introduce the window functions rec and \overline{rec} as follows:

$$rec(\mu, \nu) = \begin{cases} 1 & \text{for } |x| \leq \mu \cap |y| \leq \nu \\ 0 & \text{for } |x| > \mu \cup |y| > \nu \end{cases}, \quad (17)$$

$$\overline{rec}(\mu, \nu) = \begin{cases} 0 & \text{for } |x| \leq \mu \cap |y| \leq \nu \\ 1 & \text{for } |x| > \mu \cup |y| > \nu \end{cases}.$$

This window provides a unit region of a constant phase which is employed for arbitrary phase maps composed of a collection of the unit window cells. If we determine the phase on the pixel-by-pixel basis for a given camera device, the rectangular shape as a minimum unit cell should be a natural choice.

The intensity distribution at the focal plane is determined as a function of the peak amplitude of the probe pulse A_{0p} , the wavelength λ_p and the focal length f_p for a given Gaussian beam profile of $A_{0p}e^{-a(x_0^2+y_0^2)}$ as the probe laser. The linearly synthesized amplitude at z after crossing with the target laser pulse is expressed as

$$\psi(x_0, y_0) = \alpha \text{rec}(\mu, \nu) e^{-a(x_0^2+y_0^2)} + \beta r\bar{e}c(\mu, \nu) e^{-a(x_0^2+y_0^2)}, \quad (18)$$

where α and β are the plane waves at the point z after the penetration of the probe laser. The function α with the local phase shift δ caused by the local refractive index shift and β without phase shift are defined as

$$\begin{aligned} \alpha &= A_{0p} e^{i(kz+\delta)}, \\ \beta &= A_{0p} e^{ikz}. \end{aligned} \quad (19)$$

The Fourier transform F of the synthesized amplitude ψ on the focal plane (x, y) at z is expressed as

$$\begin{aligned} F\{\psi(x_0, y_0)\} &= \\ &\alpha F\{\text{rec}(\mu, \nu) e^{-a(x_0^2+y_0^2)}\} + \beta F\{r\bar{e}c(\mu, \nu) e^{-a(x_0^2+y_0^2)}\} \\ &= (\alpha - \beta) \int_{-\mu}^{\mu} \int_{-\nu}^{\nu} dx_0 dy_0 e^{-a(x_0^2+y_0^2)} e^{-i(\omega_x x_0 + \omega_y y_0)} + \\ &\quad \beta \int_{-\infty}^{\infty} \int_{-\infty}^{\infty} dx_0 dy_0 e^{-a(x_0^2+y_0^2)} e^{-i(\omega_y x_0 + \omega_x y_0)}, \end{aligned} \quad (20)$$

where we define $(\omega_x, \omega_y) \equiv (\frac{2\pi}{f_p \lambda_p} x, \frac{2\pi}{f_p \lambda_p} y)$. We introduce coefficient C_{sig} for the first term in (20) containing the information on how much the phase shift, namely *signal*, is localized resulted in the photon-photon interaction defined as

$$C_{sig}(\omega_x, \omega_y) \equiv \int_{-\mu}^{\mu} dx_0 e^{-ax_0^2} \cos(\omega_x x_0) \int_{-\nu}^{\nu} dy_0 e^{-ay_0^2} \cos(\omega_y y_0). \quad (21)$$

We also define coefficient C_{bkg} for the second term of (20) which corresponds to the background pedestal Gaussian part as

$$C_{bkg}(\omega_x, \omega_y) \equiv \frac{\pi}{a} e^{-\frac{(\omega_x^2 + \omega_y^2)}{4a}}. \quad (22)$$

Therefore, the Fourier transform becomes

$$F\{\psi(x_0, y_0)\} = (\alpha - \beta) C_{sig}(\omega_x, \omega_y) + \beta C_{bkg}(\omega_x, \omega_y). \quad (23)$$

By substituting (19), (21) and (22) into (23), the intensity pattern at the focal plane is expressed as

$$|\psi(\omega_x, \omega_y)|^2 = \left(\frac{A_{0p}}{f_p \lambda_p}\right)^2 \{2C_{sig}(C_{sig} - C_{bkg})(1 - \cos \delta) + C_{bkg}^2\}. \quad (24)$$

Equation (24) indicates that this method eventually corresponds to an interferometer via the cross term of $2C_{sig}(C_{sig} - C_{bkg})(1 - \cos \delta)$. This interferometer differs from the conventional one in that the modulating part due to the phase shift δ can be spatially separated from the confined strong Gaussian part C_{bkg}^2 due to the nature of C_{sig} part. Therefore, in principle, our method of sampling only peripheral intensity modulations caused by non-zero δ , provides a high signal-to-pedestal ratio circumventing the most intense focal spot. This is demonstrated in III B. See Fig.5 and 6.

We note that this method is found to be similar to but distinct from the idea in [37], where two intense target laser pulses are treated as a matterless double slit and the interference between spherical waves from these slits is discussed as a signature of the photon-photon interaction. In their proposal the physical diffraction is caused by laser-laser interaction itself. Our method rather lets the target laser cause the refractive phase shift in the probe laser as indicated in Fig.4. This phase shift is embedded in a refracted nearly plane wave in the forward direction of the probe laser as explicitly formulated in (18) and (19). We then set a lens to the right of interaction between the target and probe lasers as shown in Fig.4. The diffraction or Fourier transform in our method is incurred by the added phase of the lens component and the spherical wave propagation from the lens to the focal plane. The advantage of our method is the enhanced detectability of small phase shift on the pulse-by-pulse basis, as is demonstrated in section III B due to more efficient collection of photons by the lens effect with the simpler target geometry. On the other hand, a disadvantage is the deviation from the ideal lens phase after embedding the physical phase on the probe laser. How to correct this kind of background phase fluctuations is discussed in the following subsections.

We also note that the Fourier image on the focal plane provides only the absolute value of phase shift δ . Because of $1 - \cos \delta \sim \delta^2/2$ with $\delta \ll 1$ in (24), the proposed method has no sensitivity to the sign of phase shift in the case of almost homogeneous background phase. On the other hand, if a special offset phase $\pi/2$ is locally added along the path of the target laser before the final focusing to have the Fourier image, such setup may recover the sensitivity to the sign of phase shift, because $1 - \cos(\delta + \pi/2)$ in (24) becomes $\sim 1 + \delta$. From physical point of view, it is important to discuss whether phase shift is positive or negative, since it reflects the dynamics of local interaction. Furthermore, this has a definite advantage to enhance the signal due to the proportionality to δ compared to δ^2 for the extremely small δ . Therefore, the implementation of such local offset phase on the probe laser in advance should be a part of experimental task.

A. Template analysis for local phase reconstruction

In actual experimental situations it is unavoidable to contain local phase fluctuations inside the probe pulse on the pulse-by-pulse basis even in the absence of the physical signal. Deviations from the ideal Gaussian mode[39] and local phase fluctuations due to optical elements in the path of the probe laser may be sources of local phase fluctuations. Compared to the physical phase shift δ from the nonlinear QED effect, these fluctuations are expected to be much larger. However, if the local phase map $\phi(X)$ on each probe pulse is *a priori* measured as a function of position $X \equiv (x_0, y_0)$ on the transverse plane of the probe pulse, we may be able to correct the effect from the background fluctuations. In the next subsection III B we discuss how to measure the discrete phase map $\phi_i \equiv \phi(X_i)$ on the pulse-by-pulse basis in detail, where i denotes a discrete position on the transverse plane at which δ is embedded. Here we focus on how to determine phase shift δ from the combination of experimental data on the phase maps under such background fluctuations on the pulse-by-pulse basis.

Let us generalize the discussion of (20). The integral range in (17) included in the first of (20) can take any shape and size in general. We replace the rectangular region *rec* with the region $R_i \equiv R(X_i)$ where a constant phase is mapped within the region for the given discrete position X_i . By denoting the spatial frequency as $W = (\omega_x, \omega_y) = (2\pi x/(f_p \lambda_p), 2\pi y/(f_p \lambda_p))$ for the position on the focal plane (x, y) with the integral kernel $f(W, X) \equiv e^{-a(x_0^2 + y_0^2)} e^{-i(\omega_x x_0 + \omega_y y_0)}$, the Fourier transform including the local phase fluctuations ϕ_i is expressed as

$$\begin{aligned} \psi(W; \phi) &= F\{\psi(X; \phi)\} \\ &= \sum_i^{N_X} \{\alpha(\phi_i) - \beta\} \int_{R_i} dX f(X, W) \\ &= \sum_i^{N_X} \{\alpha(\phi_i) - \beta\} I_i(W) + \beta I_\infty(W), \end{aligned} \quad (25)$$

where N_X is the number of regions on the transverse plane at z , $\alpha(\phi_i) = A_0 e^{-i(kz + \phi_i)}$, $\beta = A_0 e^{-ikz}$, $I_i(W) = \int_{R_i} dX f(X, W)$, and $I_\infty(W) = \int_{-\infty}^{\infty} dX f(X, W)$. We note that this expression corresponds to the regional cut and paste of a Gaussian laser amplitude; *i.e.*, cutting a region with a phase determined from β at z and paste the same region by adding ϕ_i in $\alpha(\phi_i)$.

Given $\phi(X_i)$ on the pulse-by-pulse basis, we can numerically calculate the real and imaginary parts of $\psi(W; \phi)$ as follows;

$$\begin{aligned} \text{Re}\psi(W; \phi) &= \sum_i^{N_X} \{\cos(kz + \phi_i) - \cos(kz)\} I_i(W) \\ &\quad + \cos(kz) I_\infty(W), \end{aligned}$$

$$\begin{aligned} \text{Im}\psi(W; \phi) &= \sum_i^{N_X} \{\sin(kz + \phi_i) - \sin(kz)\} I_i(W) \\ &\quad + \sin(kz) I_\infty(W). \end{aligned} \quad (26)$$

The estimated background intensity pattern $I_{bkg}(\phi)$ on the focal plane with the phase fluctuations ϕ without physical phase is given by

$$I_{bkg}(W; \phi) = \{\text{Re}\psi(W; \phi)\}^2 + \{\text{Im}\psi(W; \phi)\}^2. \quad (27)$$

We now embed a template of the local physical phase shift $\delta_i \equiv \delta(X_i)$ as well. The phase shift δ_i can be evaluated from geometry of the energy density profile, *i.e.* the refractive index distribution inside the intense target laser field. This can be fixed from the experimental design on the focal spot *a priori*. We can monitor if the center of the spot is surely stable and further correct its deviation from the fixed geometry of the target laser. Given δ_i , we have to only replace the phase by $\phi_i \rightarrow \phi_i + \kappa \delta_i$ with a constant parameter κ as follows

$$\begin{aligned} I_{bkg+sig}(W; \phi + \kappa \delta) &= \\ &= \{\text{Re}\psi(W; \phi + \kappa \delta)\}^2 + \{\text{Im}\psi(W; \phi + \kappa \delta)\}^2, \end{aligned} \quad (28)$$

where *bkg + sig* refers to the fact that the physical phase is embedded in the background phase.

Given the measured intensity pattern I_{meas} on the focal plane per probe pulse focusing, we define χ^2 with (28) as a function of κ

$$\begin{aligned} \chi^2(\kappa) &\equiv \\ &= \frac{1}{N_W - 1} \sum_j^{N_W} \frac{|I_{meas}(W_j) - I_{bkg+sig}(W_j; \phi + \kappa \delta)|^2}{I_{meas}(W_j) + I_{bkg+sig}(W_j; \phi + \kappa \delta)}, \end{aligned} \quad (29)$$

where N_W is the number of sampling points on the focal plane and j runs through all discrete positions on the focal plane except for the most intense region around the focal point. We then determine the parameter κ by minimizing the χ^2 on the pulse-by-pulse basis within the acceptable accuracy. The reason why we have to determine κ on the Fourier image on the focal plane is due to the experimental constraint that we cannot sample the most intense part at the focal point. Because of the information loss at the focal point corresponding to the lower spatial frequency part, we cannot reconstruct the original phases of the probe laser before focusing by the inverse Fourier transform for the lens effect.

We note that determining κ corresponds to the measurement of the absolute value of phase shift δ . As we have discussed in the last paragraph of section III, if the offset phase $\pi/2$ is locally added to the known physical template before the focus by the lens, it provides the sensitivity to the sign of phase shift. This also has the advantage that the intensity change of the physical signal on the characteristic Fourier image is drastically enhanced due to the proportionality to δ compared to δ^2 . Such local phase may be implemented on the probe laser by

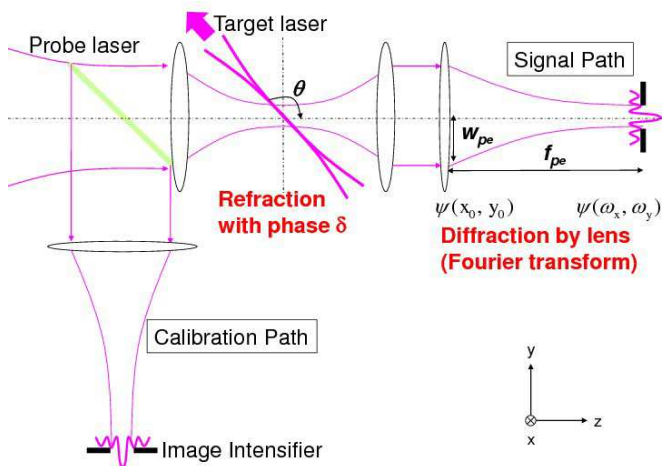


FIG. 4: Conceptual experimental setup for the suggested phase contrast Fourier imaging. At the crossing point between the probe and target lasers, the target laser causes the shift in the index of refraction, which amounts to the refractive phase shift δ embedded in the probe laser as explained in Fig.3. After the expansion from the crossing point, this probe laser goes through the lens and the signal path on the right. The diffraction or Fourier transform is incurred by the added phase of the lens component and the spherical wave propagation from the lens to the focal plane as demonstrated in Fig.2 and later in Fig.5 and 6.

utilizing the photorefractive crystal. The photorefractive effect[40] causes a static local refractive index change by supplying an external electric field onto the crystal. If we embed a rectangular shape with different refractive index on the surface of the photorefractive crystal by mimicking the shape of the target laser trajectory in vacuum, we may be able to implement the local phase offset $\pi/2$ onto the physical template in advance by making the probe laser propagate through the crystal before the final focusing by the lens. If this is the case, we can use a much weaker probe laser. In following subsections, however, we consider the case where such special offset phase is not implemented; instead, a sufficiently intense probe laser as well as the target laser is available in an experiment.

B. Suggested setup and the Fourier image

Figure 4 illustrates the conceptual experimental setup for the phase contrast Fourier imaging on the focal plane. The setup consists of two parts; the signal path (SP) and the calibration path (CP). The part SP is to perform the phase contrast Fourier imaging to measure a physically embedded phase shift by the probe-target laser interaction. Combined with SP, CP is to provide phase maps of static optical components $\phi_{opt}(X_i)$ and the phase map $\phi_{pls}(X_i)$ of probe laser brought on by instabilities in the upstream laser systems on the pulse-by-pulse basis, as we have discussed in III A.

Within SP, both the target and probe laser beams are focused with different waist sizes w_{t0} and w_{p0} with the F -number, $F_t = f_t/d$ and $F_p = f_p/d$ for the common incident beam diameter d , respectively. The lens size must be larger than d . They are crossed each other at the minimum waist point where the wave fronts in both beams are close to flat in the case of the ideal Gaussian profile beam with $R = \infty$ in (11). We assume that the target waist w_{0t} is smaller than the probe waist w_{0p} which embeds a phase contrast within the amplitude on the transverse profile of the probe laser.

The crossing angle θ has no impact on the optical length with the shift of the refractive index. However, it is important to control the amount of the refractive index shift, depending on the relevant dynamics for photon-photon interactions. In the case of QED the setting $\theta \sim \pi$ has the advantage to increase the photon-photon center of mass energy, as discussed in (16). We design the target geometry such that the Rayleigh length of the target pulse z_{Rt} is approximated as μ in (17) and the target beam waist w_{t0} is approximated as ν . Accordingly the beam waist of the probe pulse w_{p0} should coincide with z_{Rt} within the probe duration time $\tau_p = z_{Rt}/c$.

After embedding the physical phase shift onto the probe pulse at the minimum waists of both beams, the probe laser is expanded by expansion factor R_e to get the probe beam waist of w_{pe} . The expanded probe laser is refocused with the focal length f_{pe} . It is important to notice that the amount of the embedded phase contrast is independent of the rate of magnification of the transverse profile of the probe laser. This implies that we have degrees of freedom to design the final focus to produce a Fourier image with the sufficient number of photons per camera pixel that enables the pulse-by-pulse analysis, as we see below.

The procedure to determine κ by the physical interaction is as follows. First, we determine constant phase biases $\phi_{opt}(X_i)$ caused by all optical elements included in both SP and CP by performing the phase contrast Fourier imaging at the ends of CP and SP. We may assume that $\phi_{opt}(X_i)$ is stable over many pulse injections. The phase $\phi_{opt}(X_i)$ can be measured with a CW laser over a long period in between target-probe beam crossings during an experiment. Since a less intense single mode Gaussian CW laser can provide a homogeneous stable phase as the average value, we can, in principle, determine $\phi_{opt}(X_i)$ with high accuracy based on the phase contrast Fourier imaging integrated over the long time period at CP and SP by sharing the common CW laser. The template analysis discussed in III A can also be applied to this purpose. By assigning a square shape to the region R_i representing a pixel instead of the *signal* in (29), we estimate κ for each X_i . The number of photons at a point W_i on the focal plane contains convoluted phase information on the amplitude from all points on the transverse plane of the probe N_X as seen from (25). Therefore, as long as the number of sampling points on the focal plane N_W is larger than that on the transverse

probe profile N_X , we can, in principle, determine a set of $\phi_{opt}(X_i)$ from (29) by scanning κ for each X_i over the expected range of the phase variation. The achievable resolution of the phase reconstruction depends on the scanning step on κ in the χ^2 test. As we see later in Tab.I, Fig.5, and Fig.6, the phase contrast Fourier imaging at a focal plane achieves the sensitivity to the order of $\sim 10^{-7}$ in the physical phase shift by sampling only outer regions on the focal plane with a several-photon-sensitive photo device. Therefore, we can introduce the same resolution step to determine κ for $\phi_{opt}(X_i)$ as the analysis of the physical phase shift $\delta(X_i)$. We may measure the initial coarse phase map $\phi_{opt}(X_i)$ *a priori* by a typical phase resolution $\sim \lambda/100$ with a commercially available wavefront sensor. In such a case we need to repeat the two dimensional Fourier transform about 10^5 times for scanning κ for each X_i to reach the same phase resolution as $\sim 10^{-7}$ starting from the initial coarse resolution. Accordingly, a proper computing power is necessary to solve the local phases over a set of $\phi_{opt}(X_i)$. Second, we can also apply the same procedure to determine a set of $\phi_{pls}(X_i)$ on the pulse-by-pulse basis after mapping the static phase $\phi_{opt}(X_i)$ without the physical template $\delta(X_i)$ within CP. Finally, we create a phase map by adding $\phi_{opt}(X_i)$ and $\phi_{pls}(X_i)$ within SP. We then determine κ caused by the physical template $\delta(X_i)$ based on (29) with the same phase resolution step when we determined $\phi_{opt}(X_i)$ and $\phi_{pls}(X_i)$.

As a demonstration, Fig.5(top) illustrates the intensity distribution on the focal plane in SP with an arbitrary unit on the contour height in log-scale by sampling values with $50\mu\text{m}$ steps in both x and y -axes. In this figure, only the physical template $\delta(X_i)$ is embedded. The parameters used for Fig.5 are summarized in Tab.I, where the parameters for both target and probe lasers, the embedded physical phase shift due to the nonlinear QED effect, and focusing parameter after the beam expansion to obtain the Fourier transformed intensity distribution in SP are specified. Figure 5 (bottom) shows the same distribution without the physical phase shift in the 3-D plot, where the pedestal Gaussian distribution is well confined within an $20 \times 20\mu\text{m}^2$ area.

Figure 6 (top) and (bottom) show the integrated number of photons in a single target-probe crossing per $50\mu\text{m} \times 50\mu\text{m}$ pixel along the y and x -axes on the focal plane, respectively. These correspond to the photon yield per camera pixel in single pixel line along the y and x -axes, respectively in Fig.5. The plotted range is extended over ± 1 cm. In each of Fig.6, the number of photons in the peak region confined in a pixel without phase shift is overlaid. This indicates that the Gaussian pedestal part is well confined and the modulation from the physical phase shift is expanded to the outer directions on the focal plane. Therefore, by sampling only the peripheral surrounding the focal point on the focal plane without touching the most intense pedestal, we should be able to count the sufficient number of photons per pixel on the pulse-by-pulse basis. We may introduce a

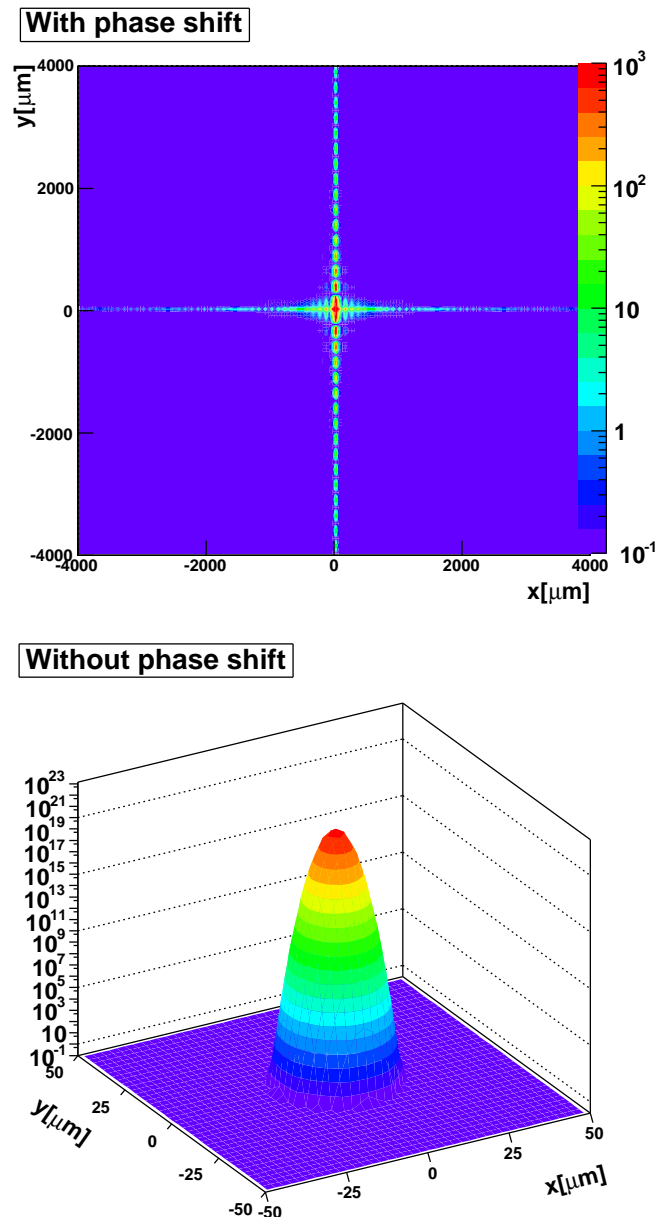


FIG. 5: Intensity profile in unit of the number of photons per single shot focusing on the focal plane by sampling the values with $50\mu\text{m}$ steps in both x and y axes. The relevant laser parameters are summarized in Tab.I. The top figure is the intensity value per point with physical phase shift based on (24). The color map is normalized to 10^3 by truncating the intensity at the focal point to zoom the signal part in the color map. The bottom plot shows the same quantity without physical phase shift in 3-D to show how much the ideal pedestal Gaussian intensity profile is localized quantitatively in the $x - y$ plane without the truncation of the intensity at the focal point.

Target laser parameters	Probe laser parameters
$\tau_t = 10$ fs	$\tau_p = z_{Rt}/c = 12$ fs
$E_t = 10$ kJ (4.03×10^{22} photons)	$E_p = 10$ kJ (4.03×10^{22} photons)
$\lambda_t = 800$ nm	$\lambda_p = 800$ nm
$F_t = 1.2$	$F_p = 4.5$
$w_{0t} = F_t \lambda_t = 0.96 \mu\text{m}$	$w_{0p} = F_p \lambda_p = 3.6 \mu\text{m}$
$z_{Rt} = \pi w_{0t}^2 / \lambda_t = 3.6 \mu\text{m}$	$z_{Rp} = \pi w_{0p}^2 / \lambda_p = 50.9 \mu\text{m}$
Embedded physical phase based on QED	
$\delta = 3.17 \times 10^{-7}$ from (16)	
$(\delta n_{qed} = 1.34 \times 10^{-8}$ from (15) with $\zeta = 7$ and $\theta = \pi/2$)	
Focusing parameter in Signal Path	
expansion factor $R_e = 5.0 \times 10^4$	
$w_{pe} = R_e w_{0p} = 18$ cm	
$f_{pe} = 5$ m	
Peak intensity $A_{pe}^2 = E_p / (2\pi w_{pe}^2)$ (1.96×10^{11} photons)	

TABLE I: Parameters to produce Fig.5 and 6 based on the conceptual experimental setup in Fig.4. The subscripts t , p and pe denotes parameters associated with the target laser, the probe laser and the probe laser after the expansion before the final focusing in the Signal Path in Fig.4, respectively. The definitions of parameters are explained in the text in section III and subsection III B. As a basic constraint on the common beam diameter d of target and probe lasers in Fig.4, we assumed $d \sim 1$ m.

several-photon sensitive photo device with an electrical amplification process such as the two-dimensional image intensifier camera. This device can increase the sensitivity to the number of countable photons and results in a higher resolution on the phase measurement. The peripheral sampling within 1cm is possible by locating flexible fiber bundles much like endoscopes with the μm precision, as already performed in a test experiment for another purpose[41].

C. Background in the phase contrast Fourier imaging

The dominant background source of the current measurement may be caused by the refractive index shift due to the plasma creation from the residual gas along the path of the focused target laser pulse. The refractive index of the static plasma in the limit of negligible collisions between charged particles is expressed as

$$N = \sqrt{1 - \frac{\omega_p^2}{\gamma \omega_0^2}}, \quad (30)$$

where ω_0 is the angular frequency of the target laser, ω_p is the plasma angular frequency defined as $\sqrt{4\pi e^2 n_e / m_e}$ and γ is the relativistic Lorentz factor given as $\sqrt{1 + a_0^2}$ with $a_0 = 0.85 \times 10^{-9} \lambda [\mu\text{m}] \sqrt{I_0 [\text{W}/\text{cm}^2]}$. In the low pressure limit of the residual gas the amount of refractive index shift ΔN is expressed as $\omega_p^2 / 2\gamma \omega_0^2$. Although the refractive index in the plasma becomes smaller than that of the peripheral area with neutral atoms, the inverted phase contrast of the phase shift inside the probe

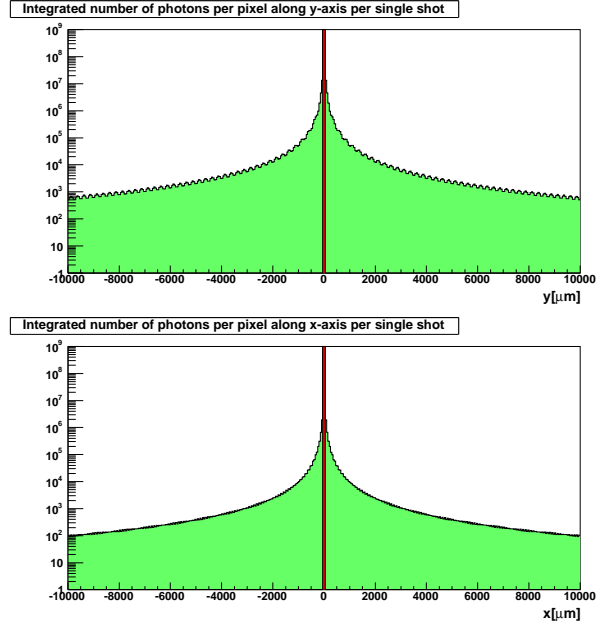


FIG. 6: The integrated number of photons over each $50 \times 50 \mu\text{m}^2$ pixel area along y (top) and x -axis (bottom) at the focal plane per single shot focusing. These correspond to the expected photon yields in a single pixel column along the y and x -axis in Fig.5. The plotted region is further extended to ± 1 cm in both axes. All relevant laser parameters are summarized in Tab.I. The ideal Gaussian pedestal distributions without physical phase shift are also superimposed on the same figures. The number of photons at the focal spot are truncated to zoom the photon yield due to phase shift. By sampling photons in regions sufficiently distant from the focal spot, one can increase the signal-to-pedestal ratio.

pulse still maintains the rectangular shape along the trajectory of the target laser. Therefore, it should produce the same characteristic diffraction pattern on the focal plane to that of the nonlinear QED case as expected from the Babinet's principle. In order to reduce this effect, we need to reduce the electron density n_e in the residual gas. If we take $\gamma \sim 1$ as the upper limit of ΔN estimate, the refractive index shift $\sim 10^{-11}$ due to the nonlinear QED effect for a reference energy density $\sim 1\text{J}/\mu\text{m}^3$, corresponding to the air pressure $\sim 10^{-6}$ Pa. This pressure is easily attainable with conventional vacuum pumps. The collisional frequency due to interactions between electrons and ions is expected to be $10^8 - 10^9 \text{s}^{-1}$ at the critical electron density $n_{cr}[\text{cm}^{-3}] = 1.12 \times 10^{21}/\lambda^2[\mu\text{m}]$ where ω_p equals ω_0 . For duration time of $\sim \text{fs}$ of the target laser pulse, the inverse bremsstrahlung radiation due to the collisional process in the residual gas is negligible at $\sim 10^{-6}$ Pa. Therefore, the dominant background contribution from the residual gas plasma can be suppressed with the pressure well below 10^{-6} Pa.

We note that what actually happens is rather more dynamical due to the pondermotive force by the high intensity laser field. In such a case the refractive index shift based on the static plasma state gives only the upper bound on the amount of the local refractive shift. As discussed in III B, we aim at the measurement of the refractive index shift on the order of $\sim 10^{-8}$ due to the nonlinear QED effect in the intensity assumed in Tab.I. This number is much greater than $\sim 10^{-11}$, as discussed above. Therefore, even if the dynamical effect is taken into account, it should be negligible to the measurement of the local refractive index shift, because the absolute value of the refractive index shift is small enough.

IV. PROBING VACUUM FIELDS IN VERY LOW ENERGIES

Extending on the QED investigation in the previous section, we now wish to explore the nonlinear vacuum response to lasers mediated by 'vacuum fields' whose energies are much lower than the energy of the pump (and probe) lasers. To the current knowledge no such fields have ever been observed. This is in spite of the fact that there are numerous theories advanced. These theories include: axions[23], minicharged particles[42-45], and dark energy[26, 27]. Why is this? This may be thought of as follows. After Rutherford's discovery of the inner core (i.e. nucleus) of an atom being very tiny compared with the size of the already tiny size of the atom, the experimental search went to explore ever smaller constituents of matter and thus the thrust for higher energy or momentum experiments. Theories have gone hand-in-hand with this exploration, succeeding in ever shorter ranged interaction theories and unification of forces, typified by the electroweak theory [46]. We have referred to this standard and extremely successful method as the high

momentum approach. Almost all laboratory research efforts have been on this approach to date. This approach, though successful in exploring high energy physics, is not suitable to explore energies much lower than eV. As mentioned in Sec.I, these fields that might exist in much lower than eV cannot strongly couple to matter, because if it did, it would have been long discovered in lower energies. Thus these fields, if they ever exist, must couple weakly. This means that we need to have an extremely strong driver to manifest a sufficient signal overcoming this weakly coupling interaction to show up above noise. We have not possessed sufficiently powerful such photon sources to date. Perhaps this may be changing now, however, with more intense laser tools are to become available [6]. What we have called the high amplitude or high field method [10, 11] may provide an alternative path to detect such low energy weakly interacting fields that are spread over semi-macroscopic scales.

When the constituent's energy is much lower than the probing photon's, it is our suggestion that we employ two laser beams in the co-propagating geometry. As we have motivated our method in the introduction, two co-parallel beams produce a very low center of mass energy interaction at the beat frequency (equal to the subtraction of the two laser frequencies) [47]. The approach is a standard Brillouin scattering of laser in matter [48-53, 55, 56]. In media such as condensed matter and plasma the utility of these two points have been recognized well in the study of nonlinear optics. For example, the Brillouin forward scattering (BFS) method [54] relies on two co-propagating laser beams with frequencies very close to each other, where the difference between these two is matched with the eigenfrequency of the acoustic modes of the medium, typically one of the lowest eigenmodes. (We note that BFS is out of a more broad class of physical processes of the parametric instabilities [51]. In addition a class of interaction under the modulational instabilities [57] shares a similar feature we may need.) It was known that this process allows strong coupling of photons to low frequency eigenmodes of the medium. This interaction could resonate with the constituent's very low eigenfrequency, should there be an eigenmode in its vicinity. Second of all, the co-propagating setup allows us to make the two beams interact over much prolonged interaction time, thus much amplifying the nonlinearities and signal arising from these.

In order to pick up the experimental signal of strong coupling to the long-range mode, however, we suggest using the second harmonic generation unlike Brillouin scattering where the detection is normally performed via the first order phonon-photon coupling. The pioneering research by Franken et al.[1] detected the nonlinearity in a quartz crystal. Two photons in co-propagation strongly interacted through the quartz fields over the coherence volume to produce the second harmonic generation. This process may be schematically looked upon as the case in Fig.7(a). There the quartz nonlinearities have mixed two forward propagating photons (ω) to produce a pho-

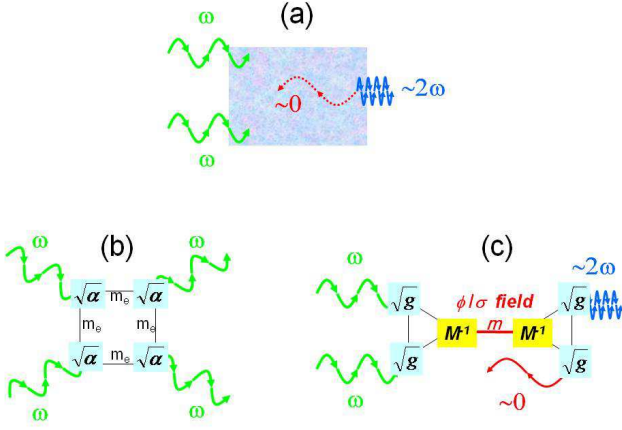


FIG. 7: Schematic diagrams of photon-photon interactions in matter and in vacuum. (a) Second harmonic generation in the experiment by Franken et al. [1], arising from the non-linearity of crystal fields irradiated by (intense enough) laser fields; (b) Probing the QED vacuum nonlinearities, as suggested by Heisenberg and Euler [31, 32], where the vertices of the coupling in the Feynman diagram are characterized by the fine structure constant of vacuum α and thus a weak nonlinearity requiring us to employ much more intense fields than the case (a). The leading order interaction is the elastic photon-photon scattering, though as a higher order there exists a second harmonic generation as well; (c) Probing potential light-mass m fields in vacuum with intense laser fields. The vertices are characterized by very feeble couplings of M^{-1} and g [27]. The expected second harmonic generation may be said to be not dissimilar to case (a). In order to increase the observable signal, suggestions have been made.

ton with 2ω (and possibly another photon with frequency ~ 0). In the previous sections we have considered nonlinear QED process (Fig.7(b)). In this two incoming photons are mediated by virtual electron-positron fields and outgoing are two photons. The extreme forward scattering amplitude with quasi-parallel incident photons is known to be largely suppressed in the QED process as we discuss later. This is because the center-of-mass energy of the colliding two photons is too low to satisfy the relevant mass scale of electron-positron pair.

In this section we consider a kinematically similar, but much more daring measurement of the photon-photon interaction mediated by low frequency "mode" of vacuum by setting up intense co-propagating lasers. As we discuss later in detail, the process we focus is based on Fig.7(c) which shows the second order in the photon-"mode" coupling. It is as if we are extending forward Brillouin scattering with the strong coupling to low frequency "mode" with the help of the resonance feature and Franken's method [1] to obtain the clearer signature to probe the second order photon-"mode" coupling.

In the previous sections, we have discussed the photon-photon interaction based on the QED process projecting for a first experimental verification of the real photon-

photon interaction in the optical wavelength range. In addition to the verification, the ratio between the first and the second term in the one-loop effective Lagrangian in (2) can yield a general test to see whether vacuum contains other effects beyond QED examining its value at 4:7. Scalar field ϕ and pseudoscalar field σ may contribute to the first and second term, respectively. Light scalar fields as a candidate of dark energy have been recently intensively discussed [26], while the pseudoscalar fields (axion-like-particles) may be a source of dark matter [23] and also possibly dark energy [25]. However, we recognize that the test in the phase contrast Fourier imaging is very limited in the mass and coupling of those fields. In this section, therefore, we extend our method to search for those new types of fields by instituting co-propagating laser beams. These endeavors may be looked upon as in Fig.7(c). Again two parallel photons come in, while two parallel photons come out. We note that our approach is similar to but distinct from many laboratory experiments with lasers [34, 58–63] already performed and proposed to search for those light fields.

Consider more details of the effective interaction Lagrangian as illustrated in the triangle part in Fig.7(c), where ϕ and σ couple to the electromagnetic field via quantum anomaly-type couplings [27]

$$\begin{aligned} -L_\phi &= g_\phi M_\phi^{-1} \frac{1}{4} F_{\mu\nu} F^{\mu\nu} \phi, \\ -L_\sigma &= g_\sigma M_\sigma^{-1} \frac{1}{4} F_{\mu\nu} \tilde{F}^{\mu\nu} \sigma. \end{aligned} \quad (31)$$

Here gM^{-1} denoted by subscript ϕ and σ for scalar and pseudoscalar fields, respectively provides the coupling strength. The dimensionless coupling g is typically proportional to the dimensionless fine structure constant α for the two photons to couple to the virtual charged particle pair in the triangle part. The effective coupling includes the large mass scale M to couple to the light field with the mass m . The large M induces the weakness of the coupling via M^{-1} . For example, the Newtonian constant G is expressed as $8\pi G = \hbar c M_P^{-2}$, where M_P is the Planckian mass of 10^{27} eV. The weakness of G is the manifestation of the large mass scale at the vertex in the triangle coupling. In what follows we abbreviate the subscripts ϕ and σ on the coupling gM^{-1} and the mass of light field m unless we need to explicitly distinguish the type of the fields. We use natural unit $\hbar = c = 1$ throughout subsequent sections, unless we explicitly note.

As a quite challenging case we have attempted a theoretical approach to search for an extremely light scalar field via the resonance in [64], which may be sensitive to the mass scale of $m_\phi \sim 10^{-9}$ eV with $M_\phi^{-1} = M_P^{-1}$ corresponding to the gravitational coupling. The method provides a new window into scoping the physics in the Planckian mass scale by photon interactions in the quasi-parallel incident laser beams in laboratories. In this section we review the essence of the approach and further develop basic formulae to apply the method to a concrete experimental setup in order to discuss reachable limits on

the coupling strength gM^{-1} and the mass m for a given laser intensity in the next section.

As illustrated in Fig.8, we introduce an unconventional coordinate frame in which two photons labeled by 1 and 2 sharing the same frequency are incident nearly parallel to each other, making an angle ϑ with the common central line along the z axis. We define the $z-x$ plane formed by \vec{p}_1 and \vec{p}_2 . The components of the 4-momenta of the photons are given by $p_1 = (\omega \sin \vartheta, 0, \omega \cos \vartheta; \omega)$ and the same for p_2 but with the sign of ϑ reversed, and $p_3 = (\omega_3 \sin \theta_3, 0, \omega_3 \cos \theta_3; \omega_3)$ and p_4 with ω_3, θ_3 replaced by $\omega_4, -\theta_4$, respectively. The angles θ_3 and θ_4 are defined also as shown in Fig.8. This coordinate system can be transformed to the center-of-mass (CM) system for the head-on collision ($\vartheta = \pi/2$) by the Lorentz transformation with $v/c \rightarrow 1$ for $\vartheta \rightarrow 0$. Conversely, this implies that the realization of the quasi-parallel collision in the laboratory frame corresponds to the realization of the extremely low CM energy, as we see below.

In this frame one of the final photons in the forward direction along the z axis must have an upshifted frequency due to the energy-momentum conservation independent of the physical origin of the dynamics. In the limit of $\vartheta \rightarrow 0$, a process of $\omega_3 \rightarrow 2\omega$ is realized. This frequency doubling nature is an extremely valuable characteristics from the experimental point of view, as compared to the case with no frequency shift in the center-of-mass system. In addition, more importantly, it is essential to maintain a quasi-parallel nature of the incident beams in order to access the resonance point, as we shall stress later.

The energy-momentum conservation laws are

$$\text{0-axis : } \omega_3 + \omega_4 = 2\omega, \quad (32)$$

$$\text{z-axis : } \omega_3 \cos \theta_3 + \omega_4 \cos \theta_4 = 2\omega \cos \vartheta, \quad (33)$$

$$\text{x-axis : } \omega_3 \sin \theta_3 = \omega_4 \sin \theta_4. \quad (34)$$

From the conditions $0 < \omega_{3,4} < 2\omega$, we may choose $0 < \theta_3 < \vartheta < \theta_4 < \pi$, without loss of generality. From (32)-(34) we derive the relation

$$\sin \theta_3 = \sin \theta_4 \frac{\sin^2 \vartheta}{1 - 2 \cos \vartheta \cos \theta_4 + \cos^2 \vartheta}. \quad (35)$$

The differential elastic scattering cross section favoring the higher photon energy ω_3 is given by

$$\frac{d\sigma}{d\Omega_3} = (8\pi\omega)^{-2} \sin^{-4} \vartheta (\omega_3/2\omega)^2 |\mathcal{M}|^2, \quad (36)$$

where \mathcal{M} is the invariant amplitude and

$$\omega_3 = \frac{\omega \sin^2 \vartheta}{1 - \cos \vartheta \cos \theta_3}. \quad (37)$$

Here we expect the upshifted frequency $\omega_3 \rightarrow 2\omega$, as $\theta_3 \rightarrow 0$ for $\vartheta \rightarrow 0$, as mentioned before.

The resonance decay rate of light fields with the mass m into two photons is expressed as

$$\Gamma = (16\pi)^{-1} (gM^{-1})^2 m^3. \quad (38)$$

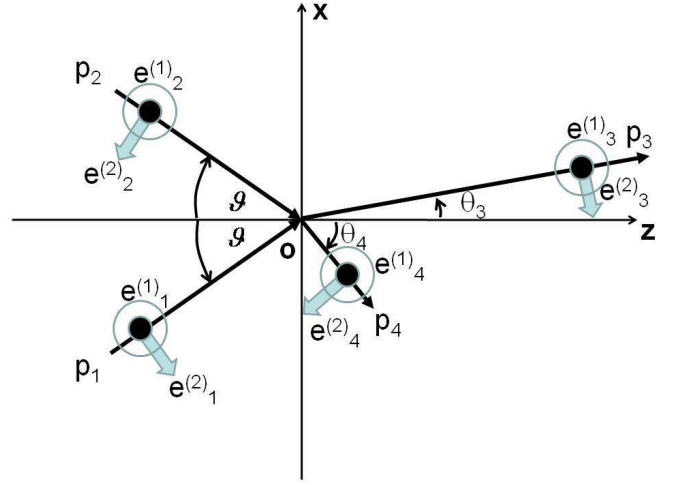


FIG. 8: Definitions of kinematical variables for the suggested co-propagating photons (this figure is quoted from [64]).

The light field is exchanged between the pairs (p_1, p_2) and (p_3, p_4) , thus giving the squared four-momentum of the scalar field

$$q_s^2 = (p_1 + p_2)^2 = 2\omega^2 (\cos 2\vartheta - 1) \quad (39)$$

with the metric convention $(+++-)$ for the definition of four momenta.

With the polarization vectors given by $\vec{e}_i^{(\beta)}$ where $i = 1, \dots, 4$ are the photon labels, whereas $\beta = 1, 2$ are for the kind of linear polarization as depicted in Fig.8, we summarize the non-zero invariant amplitudes for scalar exchanges

$$\mathcal{M}_{1111} = \mathcal{M}_{2222} = -\mathcal{M}_{1122} = -\mathcal{M}_{2211}, \quad (40)$$

and for pseudoscalar exchanges

$$\mathcal{M}_{1212} = \mathcal{M}_{1221} = -\mathcal{M}_{2112} = -\mathcal{M}_{2121}, \quad (41)$$

where the first two digits in the subscripts correspond to the states of the linear polarization of incoming two photons 1 and 2, respectively and the last two correspond to those of outgoing two photons 3 and 4, respectively as illustrated in Fig.8.

We focus on one of these non-zero amplitudes by denoting it as \mathcal{M} ;

$$\mathcal{M} = -(gM^{-1})^2 \frac{\omega^4 (\cos 2\vartheta - 1)^2}{2\omega^2 (\cos 2\vartheta - 1) + m^2}, \quad (42)$$

where the denominator, denoted by \mathcal{D} , is the light field propagator. We note q_s is timelike. We then make the replacement

$$m^2 \rightarrow (m - i\Gamma)^2 \approx m^2 - 2im\Gamma. \quad (43)$$

Substituting this into the denominator in (42), and expanding around m , we obtain

$$\mathcal{D} \approx -2(1 - \cos 2\vartheta)(\chi + ia), \quad \text{with } \chi = \omega^2 - \omega_r^2, \quad (44)$$

where

$$\omega_r^2 = \frac{m^2/2}{1 - \cos 2\vartheta}, \quad a = \frac{m\Gamma}{1 - \cos 2\vartheta}. \quad (45)$$

From (38) and (45), a is also expressed as

$$a = \frac{\omega_r^2}{8\pi} \left(\frac{gm}{M} \right)^2, \quad (46)$$

which explicitly shows the proportionality to M^{-2} . We then finally obtain the expression for the squared amplitude as

$$|\mathcal{M}|^2 \approx (2\pi)^2 \frac{a^2}{\chi^2 + a^2}. \quad (47)$$

As for the off-resonance case $\chi \gg a$, $|\mathcal{M}|^2$ is largely suppressed due to the factor $a^2 \propto M^{-4}$ for the case of small coupling M^{-1} . On the other hand, if experiments take ideally the limit of $\omega \rightarrow \omega_r$, $|\mathcal{M}|^2 \rightarrow (2\pi)^2$ is realized from (47). This is independent of the smallness of the factor M^{-4} as expected from the off-resonance case or equivalently from the square of (42). This is the most important feature arising from the resonance that overcomes the weak coupling stemming from the large relevant mass scale such as $M = M_P$. However, we then confront the extremely narrow width a for *e.g.* $gm \ll 1$ eV, $M \sim M_P = 10^{27}$ eV and $\omega_r \sim 1$ eV. We now discuss how to overcome this difficulty.

In conventional high energy collisions the beam momenta are implicitly supposed to be their mean values. This is because the momentum spread, or the uncertainty expected from the de Broglie wavelength of the relativistic particle is negligibly small compared to the relevant momentum exchanges in the interaction that experiments are interested in. Resonance searches in such experiments must adjust χ in (44) and (47) so that the mean χ is close enough to the peak location within $\pm a$. On the other hand, in the case of the co-propagating laser beam aiming at detection of extremely small momentum exchanges via the resonance, the situation is quite different due to the nature of incident waves. This is because the uncertainty included in the initial photon momenta is much larger than the relevant energy scale of the resonance, leading to the condition $|\chi| \gg a$. In this case the squared scattering amplitude must be integrated over the possible uncertainties on the incident wave function on the event-by-event basis. As we will explain below, the uncertainty in the incident photon momenta is related to the uncertainty in χ via the uncertainty in the incident angle ϑ . Therefore, it is instructive to consider the feature of the integral of the resonance function of the Breit-Wigner(BW) formula [66] from χ_- to χ_+ as follows;

$$I = \int_{\chi_-}^{\chi_+} \frac{a^2}{\chi^2 + a^2} d\chi = \left[a \tan \left(\frac{\chi}{a} \right) \right]_{\chi_-}^{\chi_+}, \quad (48)$$

where $I = a\pi/2$ and $I = a\pi$ for $\chi_+ = -\chi_- = a$ and $\chi_+ = -\chi_- = \infty$, respectively. This indicates that the

value of integral is proportional to a , *i.e.* M^{-2} from (46). The value ranges for the finite and infinite integrals over only factor of two. From this fact, we expect that the integral enhances the squared scattering amplitude by a factor of M^2 compared to the non-resonance interaction proportional to M^{-4} from (42), as long as the peak is contained within the experimental resolution on χ , *i.e.* the condition $\chi_+ > a$ and $\chi_- < -a$ is satisfied. This implies that experiments in the case of the co-propagating laser beam configuration do not have to make efforts to adjust χ close to the extremely narrow resonance region thanks to the consequent huge enhancement by the integral over the wide range on χ . Meanwhile, it is difficult to identify the exact location of the resonance mass within the wide gate on χ . Since we are interested in having the sensitivity to the extremely weak coupling such as gravity $M = M_P$, the enhancement of the squared amplitude is more crucial than finding the exact location of resonance masses. As we discuss in the following sections, however, we may be able to provide a crude estimate on the order of the mass scale of the resonance even in such a situation.

The consideration above leads us to parametrize the squared scattering amplitude as follows:

$$\begin{aligned} \overline{|\mathcal{M}|^2} &= \int_{-\infty}^{+\infty} \rho(p_1, p_2) |\mathcal{M}|^2 d\chi \\ &= (2\pi)^2 \int_{-\infty}^{+\infty} \rho(p_1, p_2) \frac{a^2}{\chi^2(p_1, p_2) + a^2} d\chi, \end{aligned} \quad (49)$$

where $\rho(p_1, p_2)$ is the normalized probability distribution to supply nominal combinations (p_1, p_2) from incident laser fields and the real part $\chi(p_1, p_2)$ is indirectly specified by (p_1, p_2) via the incident angle ϑ between incident two photons. This parametrization expresses averaging over possible combinations of p_1 and p_2 . We note that (p_1, p_2) is not *a priori* observed momenta, but just a nominal specification among the possible initial momenta. In other words, $\rho(p_1, p_2)$ is not a statistical weight on the discrete momenta after the contraction of the wavepacket of each photon state. This implies that an infinite statistics is not necessary to obtain the continuous nature. Rather, we need this treatment even for a two photon state as long as the source of photons is not the perfect plane wave. This allows the continuous integral on χ via the continuous combination of $\rho(p_1, p_2)$ in (49). As long as the probability weight $\rho(p_1, p_2)$ is close enough to unity around the resonance peak, the enhancement discussed with (48) is guaranteed. This is the essence of our main strategy of the co-propagating configuration to overcome the difficulty due to the narrow resonance width a .

In order to design experiments, we start from the resonance condition, the first of (45), by assuming $\vartheta \ll 1$,

$$m \sim 2\vartheta\omega. \quad (50)$$

We note that the product $2\vartheta\omega$ corresponds to the CM energy of incident two photons. This indicates that experiments have the two adjustable handles for a given

mass scale or the CM energy. We emphasize that we can lower the CM energy by several orders of magnitude by only introducing smaller ϑ with fixed ω . This should be contrasted to high energy colliders where we need a large amount of efforts to increase the CM energy by an order of magnitude. This advantage is also supported from a technical point of view, since scanning the incident angle ϑ should be much easier than scanning the energy ω of the resonance. We point out that the resonance condition (50) is not just at one point, but rather in a hyperbolic band in the $\vartheta - \omega$ plane given with a finite resolution with $\delta\vartheta$ of the incident angle ϑ . This implies that the deviation $\delta\omega$ from the resonance energy ω_r can satisfy the same resonance condition with a different ϑ within $\pm\delta\vartheta$. As far as $\delta\omega/\omega \ll \delta\vartheta/\vartheta$ is satisfied in the setup, we can ignore the effect of $\delta\omega$. This is in fact the case, as seen in the following discussions. Therefore, we can take the attitude that we fix the incident energy at the optical frequency $\omega = \omega_{opt}$ and scan m by changing ϑ around ϑ_r , where ω_{opt} and ϑ_r satisfy the resonance condition based on (50)

$$\omega_{opt}^2 = m^2 / (4\vartheta_r^2). \quad (51)$$

In this case the variation on ϑ leads to the variation on χ . This is expressed by the following relation based on the second of (44)

$$\chi(\vartheta) = \omega_{opt}^2 - \frac{m^2}{4\vartheta^2} = \omega_{opt}^2(1 - \varepsilon^{-2}), \quad (52)$$

where $\varepsilon \equiv \vartheta/\vartheta_r$ in the unit of ϑ_r is introduced.

We now discuss the average of the squared amplitude $|\overline{\mathcal{M}}|^2$ over the possible uncertainty on the incident angle ϑ

$$\begin{aligned} |\overline{\mathcal{M}}|^2 &= \int_0^{\pi/2} \rho(\vartheta) |\mathcal{M}|^2 d\vartheta \\ &= \int_0^{\pi/(2\vartheta_r)} \rho(\varepsilon) |\mathcal{M}|^2 \vartheta_r d\varepsilon, \end{aligned} \quad (53)$$

where $\rho(\vartheta)$ is a probability distribution function normalized between 0 and $\pi/2$ as a function of continuous uncertainty on ϑ from arbitrarily chosen two photon combinations within a laser pulse. The incident angle ϑ is re-expressed with ε with $d\vartheta = \vartheta_r d\varepsilon$ for the second of (53). From the relation (52), we find $\varepsilon = (1 - x)^{-1/2}$ and $d\varepsilon = 1/(2\omega_{opt}^2)\varepsilon^3 dx$. Equation (53) is then re-expressed with χ

$$\begin{aligned} |\overline{\mathcal{M}}|^2 &= (2\pi)^2 \frac{\vartheta_r}{2\omega_{opt}^2} \\ &\int_{-\infty}^{1-(2\vartheta_r/\pi)^2} \frac{\rho((1-\chi)^{-1/2})}{(1-\chi)^{3/2}} \frac{a^2}{(\chi^2 + a^2)} d\chi, \end{aligned} \quad (54)$$

where (47) is substituted. This equation is the exact representation of (49) starting from the uncertainty on the incident angle ϑ , if the upper limit of the integral

range is regarded as large enough compared to a . Let us define $x \equiv a\xi$ to explicitly discuss the structure of the integral kernel in the unit of the width a of BW. With ξ , (54) is further re-expressed as

$$\begin{aligned} |\overline{\mathcal{M}}|^2 &= (2\pi)^2 \frac{\vartheta_r}{2\omega_{opt}^2} a \\ &\int_{-\infty}^{a^{-1}\{1-(2\vartheta_r/\pi)^2\}} \frac{\rho((1-a\xi)^{-1/2})}{(1-a\xi)^{3/2}} \frac{1}{\xi^2 + 1} d\xi, \end{aligned} \quad (55)$$

where the first factor of the integral kernel corresponds to a normalized weight function and the second is BW with the width of unity. This expression explicitly shows the enhancement by the factor of a implying the proportionality to M^{-2} based on (46). As long as ρ is a monotonic function, the weight function in front of BW can be close to unity for small ξ because of $a\xi \ll 1$. With such a weight we expect that the value of the integral may be close to that of the BW as we discuss with a concrete weight function in the following section.

Remaining issue is how to further cope with the problem of still very small M^{-2} , though much larger than M^{-4} , in experiments. First, this can be solved by $\sin^{-4}\vartheta$ behavior of the cross section in (36) that arises from the phase volume factor and the flux factor in the quasi-parallel two photon interaction. For extremely light mass, this factor gains a large number due to small ϑ_r . Second, the intense laser fields can provide a large luminosity and the intensity of the signal is proportional to square of the intensity of laser in the limited case of the incoherent two photon interaction. We have three ingredients or knobs; the M^2 enhancement by the weighted BW integral, the factor of ϑ_r^{-4} and the growth of laser intensity. By marshalling these knobs, we expect to increase the detectability for the undiscovered light fields in vacuum, which have evaded from our grasp to date.

In the following sections we consider the experimental realizations with $\omega_r \sim 1$ eV (optical laser) and $O(1) < \vartheta_r < O(10^{-10})$ by scanning of the mass range $O(1) < m < O(10^{-10})$ eV. We then plug explicit weight functions into (55) based on the suggested experimental setup. By combining (55) and (36), we discuss reachable mass-coupling limits for a given laser intensity attainable in future experiments.

V. CONCEPTUAL LASER MEASUREMENT

We emphasized the importance of photon-photon interaction in a co-parallel or at small angle setup in order to increase the signal of detecting low energy constituents. Thus a simple way is to explore the mass range $m < \pi\omega$ by using two independent laser beams with the small incident angle. We then directly measure the resonance curve in (50) by scanning both ϑ and ω to quantitatively observe the nature of the resonance curve. For the very smaller mass scale, or equivalently smaller incident angle, however we must take into account the beam

spread in the diffraction limit. This determines the controllable smallest incident angle, or the mass scales of the light fields we look for. We consider here one-beam focusing in order to provide the simplest basis to quantify reachable mass-coupling limits for given a set of experimental parameters.

The conceptual experimental setup with one-beam focusing geometry is illustrated in Fig.9. Incident photons from a Gaussian laser pulse with linearly polarization are focused by the conceptual lens component into the diffraction limit. Quasi-parallel incident photons interact with each other between the lens and the focal point, from which photons 3 and 4 are emitted nearly in the opposite direction along the z axis with $\omega_3 \sim 2\omega$ and $\omega_4 \sim 0$. The mirror with dichroic nature is transparent to the non-interacting photons with the beam energy of ω , while ω_3 is reflected to the prism (equivalent to a group of dichroic mirrors) which selects ω_3 among residual ω and sends it to the photon detector placed off the z -axis. This process is assisted by the polarization filter. From the polarization dependence of the invariant amplitude in (40) and (41), the combinations of polarizations of two photons between the initial and final states must satisfy $11 \rightarrow 11(22)$ for the scalar field exchange and $12 \rightarrow 12(21)$ for the pseudoscalar field exchange. We note that we can choose the type of fields we search for by setting the initial polarization state. In the case of one-beam focusing the search for the scalar field is easier, because we do not have to mix the two polarization states as in the case of the pseudoscalar field. Furthermore, the selection of the rotated final state 22 can enhance the signal-to-background ratio for the scalar field case, because a huge number of non-interacting photons has the final polarization state of 11. In what follows we provide formulae to evaluate the accessible limit on the mass-coupling defined in (31) for a given laser intensity, in the case that we detect a double frequency photon per laser focusing.

The Gaussian laser parameters are summarized in (9) through (13). We now estimate the effective luminosity \mathcal{L} over the propagation volume of the laser pulse. We now restore physical dimensions of \hbar and c in this section, unless we explicitly note. Consider a Gaussian laser pulse with duration time τ with the speed of light c and the average number of photons \bar{N} per pulse. The exchange of light field may take place anywhere within the volume defined by the transverse area of the Gaussian laser times the focal length f before reaching the focal point. We first consider the effective number of photons N_{int} during an interaction with the time scale of Δt . As a result of the interaction we observe a frequency doubled photon in the laboratory frame. The momentum transfer of $\sim \hbar\omega/c$ between photons defines the minimum interaction time scale from the uncertainty principle as follows

$$\Delta t > 2\pi\omega^{-1}. \quad (56)$$

The effective number of photons during Δt is expressed

as

$$N_{int} = \frac{\Delta t}{\tau} \bar{N}. \quad (57)$$

Making the pulse duration $\tau \sim \Delta t$ maximizes the instantaneous luminosity. Suppose a point z along the laser propagation axis. The instantaneous luminosity at the point z is defined as

$$L(z) = \frac{C(N_{int}, 2)}{\pi w^2(z)} \sim \frac{N_{int}^2}{2\pi w_0^2} \frac{z_R^2}{z^2 + z_R^2} \quad (58)$$

where $C(N_{int}, 2)$ denotes a combinatorics to choose two photons among a large number of photons available within time scale of Δt and the expression of $w^2(z)$ in (10) is substituted to obtain the second with the approximation for the combinatorics. We then consider the averaged instantaneous luminosity \bar{L} over the focal length f as follows;

$$\begin{aligned} \bar{L} &= f^{-1} \int_0^f L(z) dz \sim \\ &= \frac{N_{int}^2}{2\pi f w_0^2} z_R \tan^{-1}(f/z_R) = \frac{N_{int}^2}{2f\lambda} \tan^{-1}(f/z_R). \end{aligned} \quad (59)$$

The number of effective bunches b is related with f as

$$b = \frac{f}{c\Delta t}. \quad (60)$$

The effective luminosity \mathcal{L} over the propagation volume of the laser pulse is finally expressed as

$$\begin{aligned} \mathcal{L} &= b\bar{L} \\ &= \frac{f}{c\Delta t} \frac{N_{int}^2}{2f\lambda} \tan^{-1}(f/z_R) = \frac{\Delta t}{\tau} \frac{\bar{N}^2}{2c\tau\lambda} \tan^{-1}(f/z_R), \end{aligned} \quad (61)$$

where (57) is substituted in the last step.

The uncertainty on the incident angle between two light waves is expected to be

$$\Delta\vartheta \sim \frac{\lambda}{z_R} = \pi^{-1} \left(\frac{\lambda}{w_0} \right)^2 \quad (62)$$

from the definition of the Rayleigh length $z_R = \pi w_0^2/\lambda$. The minimum beam waist w_0 at $z = 0$ varies with the experimental conditions, the focal length f , Rayleigh length z_R and diameter of conceptual lens d ,

$$w_0 = (d/2) \frac{(f/z_R)}{\sqrt{1 + (f/z_R)^2}}. \quad (63)$$

We see that $\Delta\vartheta$ may be controlled via w_0 by choosing suitable f and d in experiments.

The possible uncertainty on the incident angle ϑ affects the average of the squared amplitude $|\overline{\mathcal{M}}|^2$ as shown in the first of (53). In order to obtain an approximation close enough to reality, we plug the following step function into (53):

$$\rho(\vartheta) = \left\{ \begin{array}{ll} 1/\Delta\vartheta & \text{for } 0 < \vartheta \leq \Delta\vartheta \\ 0 & \text{for } \Delta\vartheta < \vartheta \leq \pi/2 \end{array} \right\}, \quad (64)$$

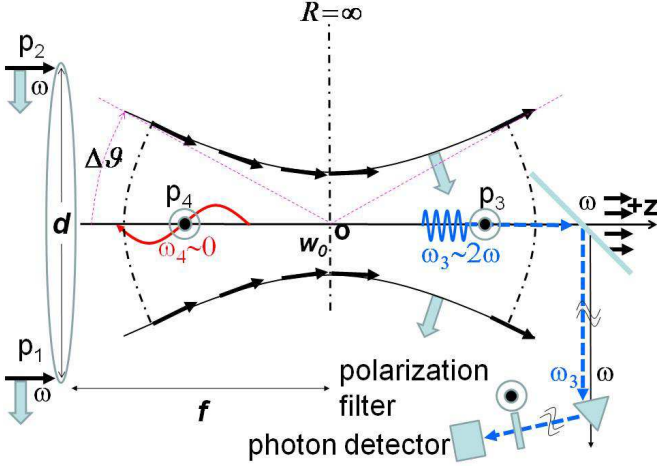


FIG. 9: Suggested experimental setup of the co-propagating photon interaction and detection. The linear polarizations of incident and outgoing photons are drawn only for the scalar exchange with the scattering amplitude $|\mathcal{M}_{1122}|$ as an example.

which is normalized to the physically possible range $0 < \vartheta \leq \pi/2$. By substituting (64) into (55), we obtain

$$\overline{|\mathcal{M}|^2} = \frac{(2\pi)^2}{2\omega_{opt}^2} \frac{\vartheta_r}{\Delta\vartheta} a \int_{-\infty}^{a^{-1}\{1-(\vartheta_r/\Delta\vartheta)^2\}} \frac{1}{(1-a\xi)^{3/2}} \frac{1}{(\xi^2+1)} d\xi, \quad (65)$$

where the first factor of the integral kernel corresponds to the weight function and the second is Breit-Wigner (BW) with the width of unity. The weight function of the kernel is close to unity for small ξ due to the smallness of a in (46). Therefore, the value of integral in (65) is almost equivalent to that of BW [65]. This is because the monotonic positive weight function approaches zero as $\xi \rightarrow -\infty$ more rapidly than the pure BW, whereas the pure BW suppresses the increase of the weight function close to zero at $\xi \rightarrow a^{-1}\{1-(\vartheta_r/\Delta\vartheta)^2\}$ for $\Delta\vartheta < 1$. We then approximate (65) as the integrated BW over $\pm \sim \infty$ as follows:

$$\overline{|\mathcal{M}|^2} \sim \frac{(2\pi)^2}{2\omega_{opt}^2} \frac{\vartheta_r}{\Delta\vartheta} a\pi. \quad (66)$$

With a in (46) and $\overline{|\mathcal{M}|^2}$ in (66), the differential cross section in (36) is finally expressed as

$$\overline{\left(\frac{d\sigma}{d\Omega_3}\right)} \sim \frac{\pi}{64} \left(\frac{2\pi}{\lambda}\right)^{-2} \left(\frac{\vartheta_r}{\Delta\vartheta}\right) \left(\frac{gm}{M}\right)^2 \vartheta_r^{-4}, \quad (67)$$

where the approximations $\omega_3 \sim 2\hbar\omega$ and $\vartheta_r \ll 1$ are taken into account.

Multiplying (61) by (67), we obtain the differential

yield per laser pulse focusing as follows:

$$\begin{aligned} \frac{dY}{d\Omega_3} &= \mathcal{L}\left(\frac{d\sigma}{d\Omega_3}\right) \\ &= \frac{1}{512\pi} \frac{\Delta t}{\tau} \frac{\lambda}{c\tau} \tan^{-1}(f/z_R) \left(\frac{\vartheta_r}{\Delta\vartheta}\right) \left(\frac{gm}{M}\right)^2 \vartheta_r^{-4} \bar{N}^2. \end{aligned} \quad (68)$$

There are several experimental knobs to affect the observable events in (68). If we choose $\tau \sim \Delta t \sim \lambda/c$ resulting in $c\tau \sim \lambda$, we can maximize the effective luminosity. From (62), the reduction of $\Delta\vartheta$ or increasing w_0 enhance the yield. From (63), we express f/z_R as

$$(f/z_R)^2 = \frac{w_0^2}{(d/2)^2 - w_0^2}. \quad (69)$$

From this relation, increasing w_0 as large as $(d/2)$ also enlarges f/z_R . This introduces a slight increase for the factor $\tan^{-1}(f/z_R)$, though its effect is tempered by the nature of \tan^{-1} .

As a short summary, we make the most important note from the experimental point of view based on this conceptual design. The condition $\vartheta_r/\Delta\vartheta = 1$ maximizes the chance to search for the resonance, while $\vartheta_r/\Delta\vartheta > 1$ results in a huge suppression of the cross section by M^{-4} ($\hbar = c = 1$) as we discussed. This is because the resonance peak is out of the region covered by $\Delta\vartheta$. This parameter corresponds to the sharp cut-off of the cross section. Therefore, controlling $\Delta\vartheta$ via relations (62), (63) and (69) can provide an experimental way to define the mass range that we eliminate if no signal is found. From the resonance condition in (50), we evaluate the lower bound on the mass range we can exclude by this conceptual design as follows ($\hbar = c = 1$):

$$\begin{aligned} m_{min} &\sim 2\vartheta_r\omega_{opt} \sim 2\Delta\vartheta\omega_{opt} \\ &= 2\pi^{-1}(\lambda/w_0)^2\omega_{opt} > 2\pi^{-1}(\lambda/d)^2\omega_{opt}, \end{aligned} \quad (70)$$

where (63) is substituted and the obvious experimental condition $w_0 < d$ is required for the last inequality. Below this lower mass bound we cannot discuss what the mass scales of the light fields are, even though the measurement is still sensitive to the presence of lighter resonances than the lower mass bound due to the large enhancement by ϑ_r^{-4} .

VI. DISCUSSION BASED ON ONE-BEAM FOCUSING

As a demonstration we now discuss the necessary laser intensity for the following reference case based on the one-beam focusing setup. First, we note that Δt in (56) is the resolvable minimum time scale. As long as we discuss extremely low mass field, the interaction time scale may be over \hbar/mc^2 . In the case of low mass the interaction time scale may be much longer than $2\pi\omega_{opt}^{-1}$. On the other hand, photon-photon interactions must occur

within τ . This fact implies we should assume $\Delta t/\tau = 1$ in the case $\Delta t > \tau$. Since the effective luminosity tends to be enhanced for smaller beam waists, we assume a short pulse laser with duration time close to $2\pi\omega_{opt}^{-1}$ in the following discussion. Let us assume that the diameter of the conceptual lens is ~ 2 m by taking the damage threshold of the lens into account for the use of high intense laser pulse. With the assumption $f \ll z_R$, the minimum beam waist in (63) is approximated as $w_0 \sim (df\lambda/(2\pi))^{1/3}$. This gives the cut-off of the sensitive mass region m_{cut} defined by the condition $\vartheta_r < \Delta\vartheta$ via the relation (62) as follows;

$$m_{cut} \equiv 2\omega_{opt}\Delta\vartheta = 2\omega_{opt}\frac{\lambda^2}{\pi(df\lambda/(2\pi))^{2/3}}. \quad (71)$$

If we are allowed to change the focal length between $\sim 1 < f < \sim 1000$ m, the cut-off mass range varies from $\sim 10^{-9}$ to $\sim 10^{-11}$ eV with $\omega_{opt} \sim 1$ eV. By choosing the focal length realizable in laboratories as $f \sim 3$ m, we expect $m_{cut} \sim 10^{-10}$ eV. For $\omega_{opt} \sim 1$ eV, the resonant incident angle is $\vartheta_r \sim 10^{-10}$ from (50). As the most challenging case, we assume the coupling as weak as gravity $M^{-1} \sim M_P^{-1}$. We are now ready to estimate the average number of photons \bar{N}_1 to expect $d\mathcal{Y}/d\Omega_3 \sim 1$ per pulse focusing based on (68) for the physical parameters: $m \sim 10^{-10}$ eV, $g \sim \alpha = 1/137$ and $M_P \sim 10^{27}$ eV, and for the experimental parameters discussed above: $\omega_{opt} \sim 1$ eV, $\tau \sim 10$ fs, $\Delta t/\tau = 1$, $w_0 \sim 0.01$ m, $d \sim 2$ m, $f \sim 3$ m, $\Delta\vartheta \sim 4 \times 10^{-9} > \vartheta_r$ and $f/z_R \sim w_0$ from (63) resulting in $\tan^{-1}(f/z_R) \sim w_0$. By taking all the factors into account, we find $\bar{N}_1 \sim \mathcal{O}(10^{22})$, corresponding to ~ 10 kJ per pulse focusing.

If the one-beam focusing setup cannot detect any signals, it excludes all of mass range below m_{cut} and all of couplings stronger than gM^{-1} in that mass range. This is because, in principle, the $\sin^{-4}\vartheta_r$ dependence in (36) enhances the cross section for the entire lower mass range below m_{cut} . We note that there is no known physical cut-off on the minimum ϑ in the photon-photon interaction. This by itself can be a subject to be studied, since it is possibly related with the texture of vacuum which may prevent the smooth propagation of photons in vacuum. This may introduce a finite cut-off in the minimum incident angle between two photons. If the intensity discussed above is available, we may be able to search for extremely light fields in the totally unprobed domain: $m < 10^{-10}$ eV and $gM^{-1} > 10^{-23}$ GeV $^{-1}$. This is a remarkable improvement compared to the axion (pseudoscalar field) searches so far taken. They provided the upper limit in the domain: $m > 10^{-6}$ eV and $gM^{-1} > 10^{-13}$ GeV $^{-1}$ [23]. The way to estimate the mass-coupling limit in our suggestion should be contrasted to the conventional ones [23] where experiments provided upper bounds on the mass-coupling limit. The gap between the two domains, however, can be filled by changing the experimental parameters in our concept. Even if there is no signals in the one-beam focusing, we only have to update the condition so that it satisfies

$\Delta\vartheta > \vartheta_r$ for heavier masses by increasing $\Delta\vartheta$. In such heavier mass region, however, two-beam crossing geometry relaxes the constraints on the optical design such as focal length. In either case the one-beam focusing setup considered in this paper provides a basis to define the mass-coupling limit as well as the necessary beam intensity as we have demonstrated here.

Our arguments above have been based on the approach in which each interaction arise incoherently yielding the observed result by $\bar{N}^2|\overline{\mathcal{M}}|^2$. It is worth noting, however, the interaction may occur coherently because the light field exchange gives a sufficiently long-range interaction, and hence individual scattering centers in the beam are indistinguishable. This coherence effect results in $\bar{N}|\bar{N}\overline{\mathcal{M}}|^2$ which is enhanced by a factor of \bar{N} over the yield expected from the incoherent summation, as was discussed in the long-wavelength neutrino interaction on a bulk target [68]. Upon more careful analysis of our system the question may be addressed if the required laser intensity can be relaxed due to a collective frequency shift rather than the shift on the single-photon basis.

A major instrumental background for the frequency doubled photon is in principle expected to be the second harmonic generation (SHG) from the final focusing optical element. The dominant source of SHG may be the interface between the residual gas and the surface of the optical element where the centrosymmetry is maximally broken. Even from the maximal estimate $\sim 10^{13}$ W/cm 2 for a typical damage threshold, we expect a negligible amount of 10^{-10} SHG photons from a 1m 2 aperture size with a 10 fs irradiation, if the optical components are housed in the vacuum containing 10^{10} atoms/cm 3 ($\sim 10^{-5}$ Pa) [67]. The confirmation of the negligible amount of the background SHG is a crucial subject for the present concept.

As a dominant physical background we expect the lowest-order QED photon-photon scattering with the forward cross section $\sim (\alpha^2/m_e^4)^2\omega^6\vartheta^4$ [69]. This turns out to be much smaller than (67) due to the distinct behavior with respect to the incident angle ϑ . This indicates the lowest-order QED contribution is negligible.

VII. CONCLUSION

We have suggested an approach to probe the nature of vacuum with intense lasers. Two main methods have been explored. The first is the phase contrast Fourier imaging at the focal plane to measure the phase shift of propagating light under the intense laser field. The second is the extremely light resonance search via higher harmonic generation by focusing a single intense laser. Both are based on similar ideas extended from those already developed to probe matter.

In these methods we take note of the nonlinearities of vacuum that are either considered to exist but at an extremely minute level or speculated to wait for our sensitive detection of an extraordinarily feeble signal. In or-

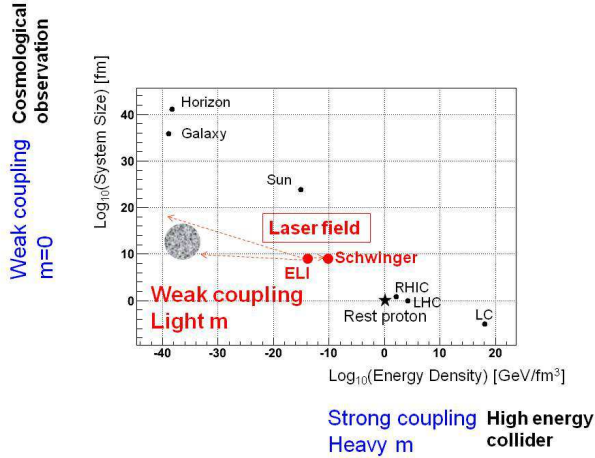


FIG. 10: Experimental ballparks of various approaches to probe matter and vacuum in the system size vs. the energy density. Selected systems are LC: electron-positron collision in the center of mass energy $E_{cms} = 1\text{TeV}$ at the future linear collider [70] assuming the electron size 10^{-18}cm , LHC: proton-proton collision in $E_{cms} = 14\text{TeV}$ at Large Hadron Collider [70], RHIC: gold-gold collision in $E_{cms} = 200\text{GeV}$ per nucleon pair at Relativistic Heavy Ion Collider [70], the rest proton indicated by the asterisk as the origin of this plot, ELI: an optical laser pulse expected in ELI project [71], Schwinger: Schwinger limit [8], Sun, the Milky Way Galaxy and event horizon with $\Omega_{tot} \sim 1.0$ and $h \equiv H_0/100[\text{km/s/Mpc}] \sim 0.7$ [72]. The energy density axis is qualitatively interpreted as the inverse of the force range or the mass scale m of exchanged force, because the mean free path becomes shorter in higher density states as long as the coupling to matter is not weak. On the other hand the coupling strength to matter gM^{-1} defined in (31) qualitatively reflects the necessary size of matter or vacuum in order to make the interaction manifest. The arrow to the higher energy density toward Schwinger limit is the direction to probe nonlinear QED interactions and also understanding of the non-perturbative nature of the intense field, while the arrows directing lower energy density region indicate the extensible domain by using co-propagating intense laser fields, since the mass range may be covered from $\sim 1\text{eV}$ to $\sim 0.1\text{neV}$ and the coupling may be probed as weak as gravitational coupling for lighter mass scales. The energy density in this direction depends on the context. In the context of the scalar field as a candidate of dark energy in [26, 64], the energy density should be close to that of the event horizon.

der to detect these weak nonlinearities, we need to spectacularly enhance the signal. The large leap in enhancing these signals is garnered by the combination of (1) the rapid development of intense laser technology and its adoption here; (2) the employment of our suggested techniques that circumvent potentially huge noise and allow the enhanced interaction with the pursued fields. The former element (1) may be brought in, for example, by the intense optical laser beyond kJ. For the latter factor (2) we have suggested for the nonlinear QED problem a method of avoiding the pedestal noise in our phase con-

trast Fourier imaging. For the exploration of possible new low mass fields we have suggested a method to hit a resonance with photons co-propagating over a long distance.

With the phase contrast Fourier imaging the nonlinear QED effects of the Euler-Heisenberg Lagrangian should be detected no more than the energy of laser around 10J. The method provides a window for scoping vacuum via the dynamics of electron mass scale virtually. Such detection has never been made to date, and it heralds the research in the physics of vacuum with the high field approach. With the detection of second harmonic generation in the co-propagating setup we should be able to survey a large sweep of the energy domain (eV to 10^{-10}eV) of the mediating vacuum fields. If and when we pick up some signal in one particular energy range, perhaps we can zoom in to this specific energy (and thus wavelength) of photons by arranging the various knobs such as the crossing angle and the (long) beat wavelength of the electromagnetic waves by setting up a specific resonance cavity, we may be able to further increase the sensitivity and more deeply study their properties.

Given the high intense optical laser beyond 1kJ per fs-pulse duration in the near future, the realization of these suggestions may become an exciting challenge for future experiments of explorations of the physics of vacuum.

Figure 10 illustrates the experimental ballparks of various approaches to probe matter and vacuum, in terms of the system size as a function of the energy density. The energy density axis is qualitatively interpreted as the inverse of the force range or the mass scale m of exchanged force in (42), because the mean free path becomes shorter in higher density state as long as the coupling to matter is relatively strong. On the other hand, the coupling to matter gM^{-1} in (42) or (31) qualitatively reflects the necessary size of matter or vacuum in order to make the interaction visible. The Galileo type telescope observes gravitational phenomena. These are on the extremely weak coupling of M_P^{-1} with zero mass exchange. High energy particle colliders, the Rutherford type microscopes focus on particle generation phenomena. These are due to strong couplings with heavy mass exchanges within fm scale. There is a huge gap between these two approaches. In other words the region of weak couplings with finite but light mass exchanges have been hardly probed so far. It is quite natural to start exploring if there exist important pieces of the puzzle of nature in these domains. These explorations might allows us deeper understanding of the nature of vacuum such as dark energy [73]. The progress of modern physics has been simply driven by those two types of the experimental approaches. The proposed method with high intense laser probes semi-macroscopic vacuum compared to particle physics and much smaller scale of vacuum compared to cosmology. Provided such semi-macroscopic vacuum scope, we increase our observational window into a new parameter regime of vacuum.

Acknowledgments

The research has been supported by the DFG Cluster of Excellence MAP (Munich-Center for Advanced Photonics). K.Homma acknowledges for support by the Grant-in-Aid for Scientific Research no.21654035 from MEXT of Japan in part. T. Tajima is the Blaise Pascal Chair of Ecole Normale Supérieure. We thank ad-

vice, collaboration, and encouragements from our colleagues, including : G. Mourou, Y. Fujii, H. Gies, R. Schützhold, G. Dunne, M. Marklund, P. Shukla, S. Bulanov, T. Esirkepov, C. Keitel, M. Siemko, R. Assmann, F. Krausz, S. Karsch, M. Zepf, S. Sakabe, K. Kondo, K. Fujii, T. Takahashi, A. Suzuki, F. Takasaki, J. Urakawa, S. Ushioda, J. Rafelski, W. Sandner, T. Heinzl, N. Naumova, and P. Chen.

-
- [1] P. Franken, A. E. Hill, C. W. Peters, and G. Weinreich, *Phys. Rev. Lett.* **7**, 118 (1961).
- [2] N. Bloembergen, *Nonlinear Optics*, (Benjamin, Reading, 1965).
- [3] L. V. Keldysh, *Sov. Phys. JETP* **20**, 1307 (1965).
- [4] T. Tajima and J. M. Dawson, *Phys. Rev. Lett.* **43**, 267270 (1979).
- [5] D. Strickland and G. Mourou, *Opt. Commun.* **56**, 219 (1985).
- [6] G. A. Mourou, T. Tajima, and S. V. Bulanov, *Reviews of Modern Physics* **78** 309 (2006).
- [7] S. V. Bulanov, T. Esirkepov, and T. Tajima, *Phys. Rev. Lett.* **91**, 085001 (2003).
- [8] J. Schwinger, *Phys. Rev.* **82**, 664 (1951).
- [9] M. Marklund and P. K. Shukla, *Reviews of Modern Physics* **78** 591 (2006).
- [10] Tajima T., Mima K., Baldis H. eds., *High Field Science* (Kluwer Academic/Plenum, New York, 2000).
- [11] T. Tajima, *Eur. Phys. J. D* **55** 519-529 (2009).
- [12] D. Cremers and L. Radziemski, *Handbook of Laser-Induced Breakdown Spectroscopy* (J. Wiley & Sons, London, 2006).
- [13] J. S. Toll, *The Dispersion Relation for Light and its Application to Problems Involving Electron Pairs*, PhD thesis, Princeton, 1952.
- [14] N. B. Narozhnyi, *Sov. Phys. JETP* **28**, 371 (1969).
- [15] V. I. Ritus, *Ann. Phys.* **69**, 555 (1972).
- [16] W. Dittrich and H. Gies, *Probing the Quantum Vacuum* (Springer, Berlin, 2007).
- [17] G. M. Shore, *Nucl. Phys. B* **778**, 219 (2007) [arXiv:hep-th/0701185].
- [18] T. Heinzl and A. Ilderton, *Eur. Phys. J. D* **55**, 359 (2009) [arXiv:0811.1960 [hep-ph]].
- [19] G. V. Dunne, H. Gies and R. Schützhold, *Phys. Rev. D* **80**, 111301 (2009) [arXiv:0908.0948 [hep-ph]].
- [20] V. N. Baier and V. M. Katkov, *Phys. Lett. A* **374**, 2201 (2010) [arXiv:0912.5250 [hep-ph]].
- [21] N. B. Narozhny, *Zh. Eksp. Teo. Fiz.* **54**, 676 (1968).
- [22] J. F. Gunion, H. E. Haber, G. L. Kane and S. Dawson, *The Higgs Hunters's Guide*, BNL-41644.
- [23] See section for *Axions and other similar particles* in C. Amsler et al. (Particle Data Group), *Phys. Lett. B* **667**, 1 (2008) and 2009 partial update for the 2010 edition.
- [24] L. Maiani, R. Petronzio and E. Zavattini, *Phys. Lett. B* **175**, 359 (1986); G. Raffelt and L. Stodolsky, *Phys. Rev. D* **37**, 1237 (1988).
- [25] H. J. de Vega and N. G. Sanchez, astro-ph/0701212.
- [26] Y. F. Cai, E. N. Saridakis, M. R. Setare and J. Q. Xia, arXiv:0909.2776 [hep-th]; S. Tsujikawa, arXiv:1004.1493 [astro-ph.CO].
- [27] Y. Fujii and K. Maeda, *The Scalar-Tensor Theory of Gravitation* (Cambridge Univ. Press, 2003).
- [28] R. Karplus and M. Neuman, *Phys. Rev.* **83** 776-784 (1950).
- [29] B. De Tollis, *Nuovo Cimento* **32** 757 (1964); B. De Tollis, *Nuovo Cimento* **35** 1182 (1965).
- [30] R. Schützhold, H. Gies and G. Dunne, *Phys. Rev. Lett.* **101**, 130404 (2008) [arXiv:0807.0754 [hep-th]]; N. B. Norozhny, *Sov. Phys. JETP* **27**, 360 (1968).
- [31] W. Heisenberg and H. Euler, *Z. Phys.* **98**, 714 (1936) [arXiv:physics/0605038].
- [32] V. Weisskopf, *Kong. Dans. Vid. Selsk. Math-fys. Medd.* **XIV**, 166 (1936).
- [33] M. L. Goldberger and K. M. Watson, *Collision Theory* (Jon Wiley and Sons, NY, 1964)
- [34] E. Zavattini *et al.* [PVLAS Collaboration], *Phys. Rev. D* **77**, 032006 (2008) [arXiv:0706.3419 [hep-ex]].
- [35] A. N. Luiten and J. C. Petersen, *Phys. Rev. A* **70**, 033801 (2004).
- [36] A. Di Piazza, K. Z. Hatsagortsyan and C. H. Keitel, *Phys. Rev. Lett.* **97**, 083603 (2006) [arXiv:hep-ph/0602039].
- [37] B. King, A. Di Piazza and C. H. Keitel, *Nature Photonics* **4** (2010), 92.
- [38] A. E. Siegman, *Lasers* (University Science Books, California, 1986).
- [39] For example, references are found in B. Quesnel and P. Mora, *Phys. Rev. E* **58**, 3719 (1998).
- [40] Amnon Yariv, *Optical Electronics in Modern Communications* (Oxford University Press, Inc., Oxford, 1997).
- [41] K. Homma and K. Hosokawa, *Proc. INPC2007 vol.II* 609-611.
- [42] B. Holdom, *Phys. Lett. B* **166**, 196 (1986).
- [43] B. Batell and T. Gherghetta, *Phys. Rev. D* **73**, 045016 (2006) [arXiv:hep-ph/0512356].
- [44] S. A. Abel, J. Jaeckel, V. V. Khoze and A. Ringwald, *Phys. Lett. B* **666**, 66 (2008) [arXiv:hep-ph/0608248].
- [45] H. Gies, J. Jaeckel and A. Ringwald, *Phys. Rev. Lett.* **97**, 140402 (2006) [arXiv:hep-ph/0607118].
- [46] S. Weinberg, *Phys. Rev. Lett.* **19**, 1264 (1967).
- [47] A. T. Forrester, R. A. Gudmundsen, and P. O. Johnson, *Phys. Rev.* **99**, 1691 (1955); Y. Minami, T. Yogi and K. Sakai, *Phys. Rev. A* **78**, 033822 (2008).
- [48] L.Brillouin, *Ann. Phys. (Paris)* **17**, 88 (1922).
- [49] R. Chiao, C. Townes, and B. Stoicheff, *Phys. Rev. Lett.* **12**, 592 (1964).
- [50] A. Maradudin and E. Burstein, *Phys. Rev.* **164**, 1081 (1967).
- [51] K. Nishikawa, *J. Phys. Soc. Japan* **24**, 1152 (1968).
- [52] M. Rosenbluth, *Phys. Rev. Lett.* **29**, 565 (1972).
- [53] W. Kruer, *The physics of laser plasma interactions*, (Addison-Wesley, Reading, 1988).
- [54] T. Tajima, *Laser Part. Beams* **3**, 351 (1985).

- [55] LLE (Laboratory for Laser Energetics) Review, ed. R. Epstein (Univ. of Rochester, Rochester, 1998) p. 189.
- [56] C. McKinstrie and E. Startsev, Phys. Rev. E **60**, 5978 (1999).
- [57] P. Sprangle, J. Krall, and E. Esarey, Phys. Rev. Lett. **73**, 3544 (1994); M. Centurion et al., Phys. Rev. A **75**, 063804 (2007).
- [58] R. Cameron *et al.*, Phys. Rev. D **47**, 3707 (1993).
- [59] C. Robilliard, R. Battesti, M. Fouche, J. Mauchain, A. M. Sautivet, F. Amiranoff and C. Rizzo, Phys. Rev. Lett. **99**, 190403 (2007) [arXiv:0707.1296 [hep-ex]]; M. Fouche *et al.*, Phys. Rev. D **78**, 032013 (2008) [arXiv:0808.2800 [hep-ex]].
- [60] K. Ehret *et al.*, arXiv:hep-ex/0702023.
- [61] A. V. Afanasev, O. K. Baker and K. W. McFarlane, arXiv:hep-ph/0605250; A. Afanasev *et al.*, Phys. Rev. Lett. **101**, 120401 (2008) [arXiv:0806.2631 [hep-ex]].
- [62] P. Pognat *et al.* [OSQAR Collaboration], Phys. Rev. D **78**, 092003 (2008) [arXiv:0712.3362 [hep-ex]].
- [63] A. S. Chou *et al.* [GammeV (T-969) Collaboration], Phys. Rev. Lett. **100**, 080402 (2008) [arXiv:0710.3783 [hep-ex]]; A. S. Chou *et al.* [GammeV Collaboration], Phys. Rev. Lett. **102**, 030402 (2009) [arXiv:0806.2438 [hep-ex]].
- [64] Y. Fujii and K. Homma, arXiv:1006.1762 [gr-qc].
- [65] The complicated analytic solution of the integral is found. We have checked the behavior of the solution around the width a .
- [66] For example, see section for *Cross-section formulae for specific processes* in C. Amsler et al. (Particle Data Group), Phys. Lett. **B667**, 1 (2008) and 2009 partial update for the 2010 edition.
- [67] V. G. Bordo, Optics Communications **132**, 62-72 (1996).
- [68] P. F. Smith, IL Nuovo Cimento **83A**, 263 (1984).
- [69] See p.183 in W. Dittrich and H. Gies, *Probing the Quantum Vacuum* (Springer, Berlin, 2007).
- [70] See section for *High-energy collider parameters* in C. Amsler et al. (Particle Data Group), Phys. Lett. **B667**, 1 (2008) and 2009 partial update for the 2010 edition.
- [71] <http://www.extreme-light-infrastructure.eu/>.
- [72] D. N. Spergel et al., Astrophysical Journal Supplement, **148**, 175 (2004)
- [73] A. G. Riess, et al. Astron. J. **116**, 1009 (1998); S. Perlmutter, et al. Nature **391**, 51 (1998).